Rapport de la réunion d'automne de la SSP

Autor(en): **Perrier, Jacques**

Objekttyp: **AssociationNews**

Zeitschrift: **Helvetica Physica Acta**

Band (Jahr): **64 (1991)**

Heft 2

PDF erstellt am: **22.07.2024**

Nutzungsbedingungen

Die ETH-Bibliothek ist Anbieterin der digitalisierten Zeitschriften. Sie besitzt keine Urheberrechte an den Inhalten der Zeitschriften. Die Rechte liegen in der Regel bei den Herausgebern.
Die auf der Plattform e-periodica veröffentlichten Dokumente stehen für nicht-kommerzielle Zwecke in Lehre und Forschung sowie für die private Nutzung frei zur Verfügung. Einzelne Dateien oder Ausdrucke aus diesem Angebot können zusammen mit diesen Nutzungsbedingungen und den korrekten Herkunftsbezeichnungen weitergegeben werden.
Das Veröffentlichen von Bildern in Print- und Online-Publikationen ist nur mit vorheriger Genehmigung der Rechteinhaber erlaubt. Die systematische Speicherung von Teilen des elektronischen Angebots auf anderen Servern bedarf ebenfalls des schriftlichen Einverständnisses der Rechteinhaber.

Haftungsausschluss

Alle Angaben erfolgen ohne Gewähr für Vollständigkeit oder Richtigkeit. Es wird keine Haftung übernommen für Schäden durch die Verwendung von Informationen aus diesem Online-Angebot oder durch das Fehlen von Informationen. Dies gilt auch für Inhalte Dritter, die über dieses Angebot zugänglich sind.

Ein Dienst der *ETH-Bibliothek*
ETH Zürich, Rämistrasse 101, 8092 Zürich, Schweiz, www.library.ethz.ch

http://www.e-periodica.ch

Helvetica Physica Acta
Vol. 64 (1991)

0018-0238/91/020159-52$1.50+0.20/0

Results from the L3 Experiment

Jacques Perrier

Département de Physique Nucléaire et Corpusculaire
Université de Genève, 1211 Genève 4, Switzerland

This talk is intended for non-specialists of high energy physics, curious of the results obtained by the L3 experiment in its first year of running at the CERN **L**arge **E**lectron-**P**ositron collider.

Since the first collisions in August 1989, the L3 detector (Ref. 1) has recorded about 150000 Z^0 decays. The analysis of these data has produced a wealth of results. Among the most important ones, I shall discuss the measurements of the mass and total width of the Z^0, the determination of the number of light neutrino species, and the measurement of the Z^0 partial widths to charged leptons. Finally, we shall see how these results are used in a precision test of electroweak theory.

Electroweak theory groups spin-$\frac{1}{2}$ fundamental fermions into doublets of leptons and doublets of quarks. Fermions appear in families made of one doublet of leptons and one doublet of quarks. Up to now three families have been observed (Table 1). The third family is not complete.

Table 1.

	Leptons		*Quarks*	
1^{st} *family*	e^-	ν_e	d	u
2^{nd} *family*	μ^-	ν_μ	s	c
3^{rd} *family*	τ^-	ν_τ	b	**t**

The top quark (t) has not been observed, most probably because of its large mass. The electroweak theory does not predict the mass of the top quark, neither the number of families. The electroweak interaction between fermions is mediated by four spin-1 vector bosons: the photon (electromagnetic interaction) and the Z^0, W^+, and W^- bosons (weak interaction). The first few years of LEP are dedicated to the study of the Z^0 properties. From 1994, the energy of LEP will be increased to produce pairs of W^+W^- bosons.

The Z^0 decays into pairs of fermion-antifermion with mass $m_f < \frac{1}{2}M_{Z^0}$. If there are no more than three families, we expect the Z^0 to decay $\sim 10\%$ of the time into charged leptons (e^+e^-, $\mu^+\mu^-$, and $\tau^+\tau^-$), $\sim 20\%$ into $\nu\bar{\nu}$, and $\sim 70\%$ into $quark - antiquark$ ($d\bar{d}$, $u\bar{u}$,... but not $t\bar{t}$). The Z^0 total width, the inverse of its average lifetime, is the sum of its partial widths over all allowed decay modes: $\Gamma_{Z^0} = \frac{\hbar}{\tau} = \Gamma_{e^+e^-} + \Gamma_{\nu_e\bar{\nu}_e} + \Gamma_{u\bar{u}} + \cdots$. The measurement of a larger width would signal the existence of new decay modes.

Z^0 Mass and Total Width

For these precision measurements we have used $e^+e^- \to q\bar{q}$ events ($q \equiv quark$) which constitute the bulk of our data. These events can occur through electromagnetic or weak current interactions (Fig. 1). The weak neutral-current, $J_\mu^{weak} = \bar{f}(g_V^{(f)}\gamma_\mu + g_A^{(f)}\gamma_\mu\gamma^5)f$,

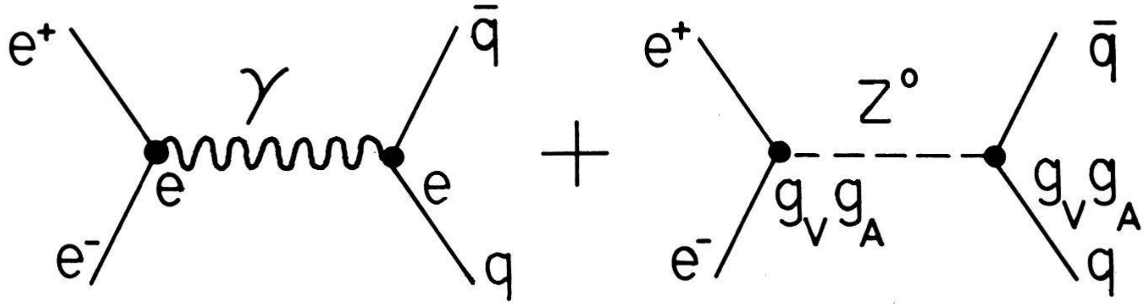

Figure 1. Lowest order contributions to $e^+e^- \rightarrow q\bar{q}$.

contains two terms that transform as a vector and an axial-vector, with couplings $g_V^{(f)}$ and $g_A^{(f)}$, respectively. These couplings depend upon the type of fermion and are function of $sin^2\theta_W$, one of the fundamental parameters of the electroweak theory. The $e^+e^- \rightarrow q\bar{q}$ total cross section has the following form:

$$\sigma(s) = \frac{4\pi Q_q^2\alpha^2}{s} + \frac{s}{(s-M_{Z^0}^2)^2 + M_{Z^0}^2\Gamma_{Z^0}^2}\left[\frac{12\pi\Gamma_{ee}\Gamma_{q\bar{q}}}{M_{Z^0}^2} + \frac{3I_q(s-M_{Z^0}^2)}{s}\right] \tag{1}$$

where s is the square of the energy in the center-of-mass of the collision, Q_q is the charge of the quark, and α is the fine structure constant. The first term is the pure electromagnetic cross section and decreases as $1/s$. The second term shows a resonance behaviour. For center-of-mass energies close to M_{Z^0}, the cross section is totally dominated by this weak interaction term. The third term is the result of the interference between the electromagnetic and weak amplitudes. The shape of the total cross section depends upon the values of the Z^0 mass and width. To measure this shape, we have scanned the Z^0 resonance by changing the energy of LEP step by step. At each step, the rate of $e^+e^- \rightarrow q\bar{q}$ events is measured. The total cross section is deduced from the measured rate, taking into account the luminosity of LEP. Quarks are subject to strong interactions and do not exist as free particle. They manifest themselves in e^+e^- annihilations as jets of particles. A typical $e^+e^- \rightarrow q\bar{q}$ event is shown in Fig. 2 (projection normal to the beam axis). The two jets produced by the quark and the antiquark are clearly visible in the central tracking chamber (A). Most of the particles in the jets interact and deposit their energies in the electromagnetic (B) and hadronic calorimeters (C). Hadronic events, like this one, can be easily identified by the jets in the tracking chamber and by a total observed energy almost equal to the center-of-mass energy. Our measured total cross section is shown in Fig. 3 (black dots). The Z^0 mass and total width are determined from a fit to this cross section (Ref. 2):

$$M_{Z^0} = 91.164 \pm 0.033\ GeV \qquad \Gamma_{Z^0} = 2.492 \pm 0.025\ GeV$$

As we shall see, the high precision of the mass measurement, 0.03%, is essential for precision test of electroweak theory. The value of the total width is also particularly interesting as it allows a precise determination of the number of light neutrino species.

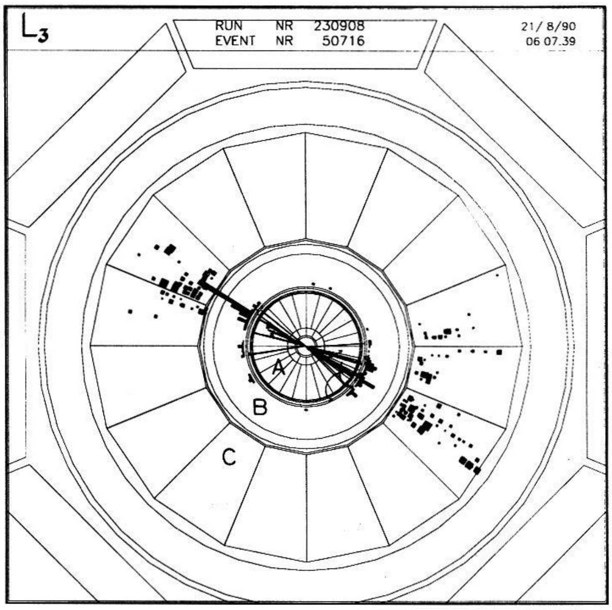

Figure 2. Typical $e^+e^- \to q\bar{q}$ event.

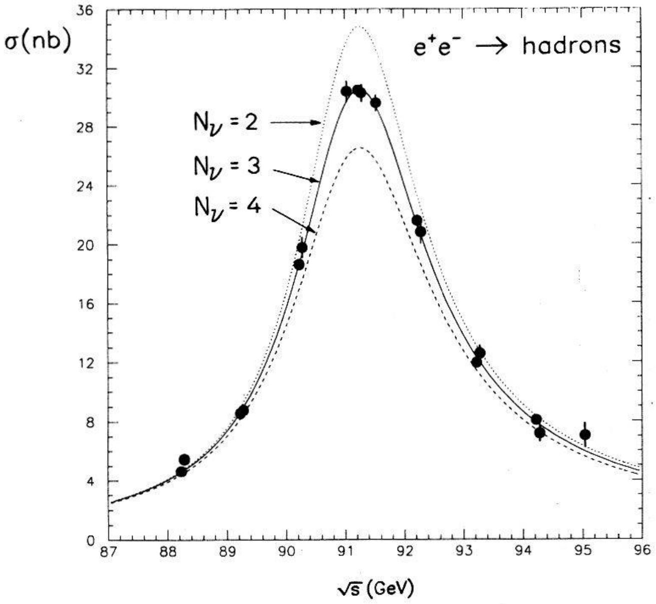

Figure 3. $e^+e^- \to q\bar{q}$ total cross section: Data (black dots) and electroweak theory expectations for 2, 3, and 4 light neutrino species.

Number of Light Neutrino Species

For three families, the electroweak theory predicts $\Gamma^{(3)}_{Z^0} = 2.490\ GeV$. If there is a fourth family with light neutrino, $m_{\nu_4} \ll \frac{1}{2}M_{Z^0}$, the decay $Z^0 \to \nu_4\bar{\nu}_4$ would occur and the Z^0 total width would be larger by $\Gamma_{\nu\bar{\nu}} = 0.166\ GeV$ giving $\Gamma^{(4)}_{Z^0} = 2.656\ GeV$. From these predictions and from our measured value, $\Gamma_{Z^0} = 2.492 \pm 0.025\ GeV$, we determine the number of light neutrino species: $N_\nu = 3.01 \pm 0.11$ (Ref. 2). This is even more dramatic when we consider the shape of the cross section (Fig. 3). The largest effect is on the maximum value of the cross section as $\sigma^{peak} \propto 1/\Gamma^2_{Z^0}$. With the assumption that all neutrinos are light, this limits the number of families to three, and the number of fundamental fermions to twelve.

$Z^0 \to e^+e^-$, $\mu^+\mu^-$, and $\tau^+\tau^-$ Partial Widths

The measurement of these partial widths provides a determination of the electroweak parameter $sin^2\theta_W$. At lowest order, the electroweak theory predicts

$$\Gamma_{ll} = \frac{\mathrm{G_F M^3_{Z^0}}}{6\sqrt{2}\pi}(g_A^2 + g_V^2) \tag{2}$$

with $g_A = -\frac{1}{2}$ and $g_V = -\frac{1}{2} + 2sin^2\theta_W$. $\mathrm{G_F}$ is the well-known Fermi coupling constant. We expect identical values for Γ_{ee}, $\Gamma_{\mu\mu}$, and $\Gamma_{\tau\tau}$ (lepton universality). The partial widths are obtained from the total cross sections $e^+e^- \to e^+e^-$, $\mu^+\mu^-$, and $\tau^+\tau^-$.

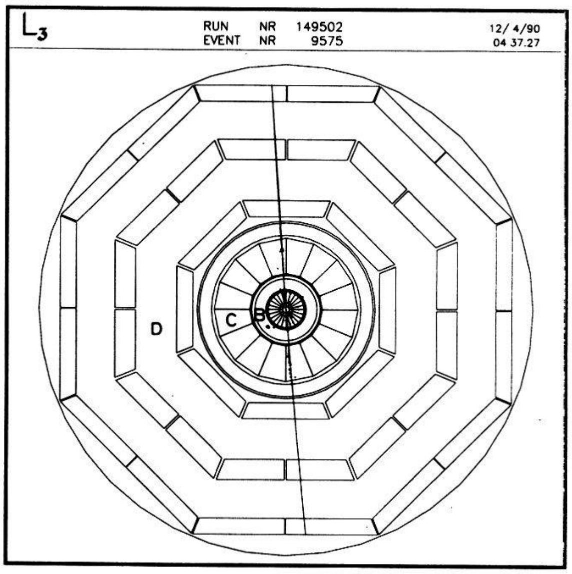

Figure 4. Typical $e^+e^- \to \mu^+\mu^-$ event.

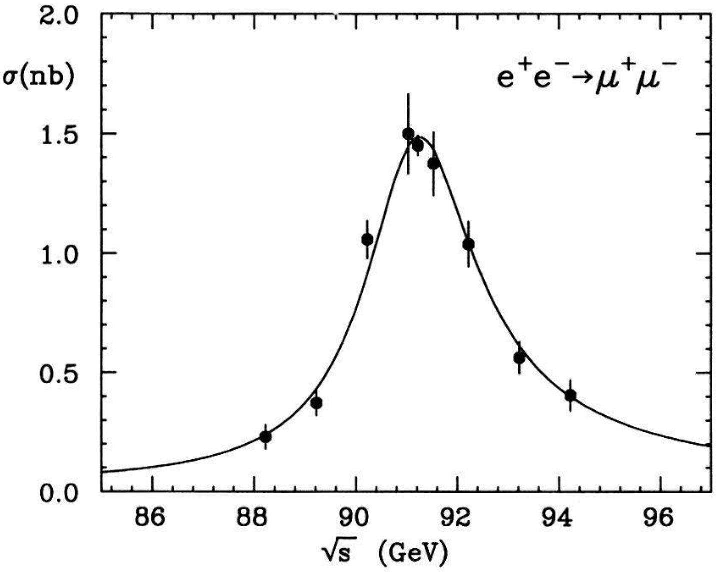

Figure 5. $e^+e^- \to \mu^+\mu^-$ total cross section. Data: black dots; Fit: continuous line.

For example, a fit to the $e^+e^- \to \mu^+\mu^-$ total cross section

$$\sigma(s) = \frac{4\pi Q_q^2 \alpha^2}{3s} + \frac{s}{(s - M_{Z^0}^2)^2 + M_{Z^0}^2 \Gamma_{Z^0}^2} \left[\frac{12\pi \Gamma_{ee} \Gamma_{\mu\bar{\mu}}}{M_{Z^0}^2} + \frac{I_\mu (s - M_{Z^0}^2)}{s} \right] \tag{3}$$

yields $\Gamma_{ee}\Gamma_{\mu\mu}$. Similarly, Γ_{ee} and $\Gamma_{ee}\Gamma_{\tau\tau}$ are obtained from fits to the e^+e^- and $\tau^+\tau^-$ total cross sections. A simultaneous fit to all three cross sections provides directly Γ_{ee}, $\Gamma_{\mu\mu}$, and $\Gamma_{\tau\tau}$.

The decays of the Z^0 into charged leptons can be easily identified. For example, $e^+e^- \to \mu^+\mu^-$ events (Fig. 4) are characterized by two back-to-back high momentum tracks crossing the entire detector and by very small deposits of energy in the calorimeters. The $e^+e^- \to \mu^+\mu^-$ total cross section is shown in Fig. 5. Similar results have been obtained for e^+e^- and $\tau^+\tau^-$ (Ref. 3). A simultaneous fit to the cross sections yields $\Gamma_{ee} = 84.3 \pm 1.6\ MeV$, $\Gamma_{\mu\mu} = 82.3 \pm 2.9\ MeV$, and $\Gamma_{\tau\tau} = 83.5 \pm 3.7\ MeV$, which verifies lepton universality. Assuming $\Gamma_{ee} = \Gamma_{\mu\mu} = \Gamma_{\tau\tau}$, we get $\Gamma_{ll} = 84.0 \pm 1.2\ MeV$. We could now compute $sin^2\theta_W$ using Eq. 2. However, for a precise determination of $sin^2\theta_W$ radiative corrections have to be taken into account. This leads to a redefinition of the fundamental parameters of the electroweak theory (replacement of coupling constants by "running" coupling constants: $\alpha \to \bar{\alpha}$, $sin^2\theta_W \to sin^2\bar{\theta}_W$) and to new relations between experimentally measured quantities and parameters (Ref. 4). Eq. 2 becomes

$$\Gamma_{ll} = \frac{\mathrm{G_F M_{Z^0}^3}}{6\sqrt{2}\pi}\ \rho \left((-\frac{1}{2})^2 + (-\frac{1}{2} + 2sin^2\bar{\theta}_W)^2 \right) \tag{4}$$

with $\rho = 1 + \frac{3\sqrt{2}\mathrm{G_F}}{16\pi^2} m_{top}^2$. The mass of the unobserved top quark must be specified in order to determine $sin^2\theta_W$ precisely ! With an additional relation, we would be able to determine $sin^2\bar{\theta}_W$ and m_{top}. More relations would test the consistency of the electroweak theory.

Precision Test of Electroweak Theory

Application of the electroweak theory to determination of the muon lifetime leads to the relation

$$\rho\, M_{Z^0}^2\, sin^2\bar{\theta}_W\, (1 - sin^2\bar{\theta}_W) = \frac{\pi\bar{\alpha}}{\sqrt{2}\mathrm{G_F}} \tag{5}$$

Another relation links $sin^2\bar{\theta}_W$ to the ratio of the vector boson masses

$$sin^2\bar{\theta}_W = 1 - \frac{1}{\rho}\left(\frac{M_W}{M_{Z^0}}\right)^2 \tag{6}$$

Relations (4), (5), and (6) restrict the values of $sin^2\bar{\theta}_W$ and m_{top} to three different regions (Fig. 6). The sizes of these regions depend upon the precision achieved on the experimentally measured quantities: $\bar{\alpha}$, $\mathrm{G_F}$, Γ_{ll}, M_{Z^0}, and M_W. Particularly on Γ_{ll}, M_{Z^0}, and M_W as $\bar{\alpha}$ and $\mathrm{G_F}$ are known with almost negligible errors. Today, the best measurements of $\frac{M_W}{M_{Z^0}}$ come from the CERN and Fermilab (U.S.A.) proton-antiproton colliders. This may change when LEP starts producing $W^\pm$ bosons in 1994. The likeliest values of $sin^2\bar{\theta}_W$ and m_{top} are: $sin^2\bar{\theta}_W = 0.230 \pm 0.004$ and $m_{top} = 137 \pm 40$ GeV (L3 data, Ref. 3). Note that this value of $sin^2\bar{\theta}_W$ agrees with previous determinations and that the top quark mass is compatible with the lower limit set by Fermilab, $m_{top} > 89$ GeV.

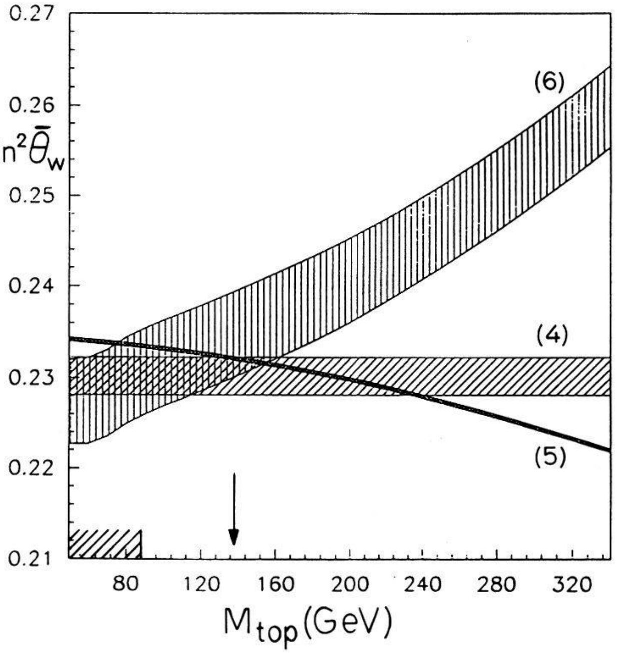

Figure 6. Constraints on ($sin^2\bar{\theta}_W$,m_{top}): (4) and (5): average LEP data; (6) CERN and Fermilab $p\bar{p}$ data (plot: M. Martinez, CERN).

In the next few years, significant improvements in the measurements of Γ_{ll} and $\frac{M_W}{M_{Z^0}}$ are expected from LEP. This will lead to even more stringent tests of electroweak theory. But up to now, all measurements agree with the standard theory of electroweak interactions.

References

[1] "The Construction of the L3 Experiment",
L3 Collaboration, Nucl. Instr. Meth. A289, 35 (1990).

[2] "A Precision Measurement of the Number of Neutrino Species",
L3 Collaboration, Preprint no. 9, July 14 (1990), submitted to Phys. Lett. B.

[3] "A Determination of Electroweak Parameters from $Z^0 \to \mu^+\mu^-(\gamma)$",
L3 Collaboration, Phys. Lett. 247B, 473 (1990).
"A Determination of Electroweak Parameters from Z^0 Decays into Charged Leptons",
L3 Collaboration, Preprint no. 17, August 20 (1990), submitted to Phys. Lett. B.

[4] See, for example, "Z Physics at LEP 1", CERN Yellow Report 89-08, September 1989,
Ed. by G. Altarelli, R. Kleiss, and C. Verzegnassi.

Gradient corrections in 3d magnetic materials.

B.Barbiellini[1],E.G.Moroni[2] and T.Jarlborg[1]

[1]DPMC,Université de Genève,CH-1211 Genève 4,Switzerland.
[2]Université de Lausanne and IRRMA,CH-1015 Lausanne,Switzerland.

The effect of Perdew Wang (PW) gradient corrections on local density potentials are calculated for Fe, Ni and Fe_3Ni. It is found that the separation between magnetic and non magnetic states is increased both in total energy and volume. While the PW potential predicts the correct structure for Fe, it cannot lead to the conventional explanation for the Invar effect in Fe_3Ni.

It is well known, that for different 3d transition metals and their alloys the LSDA shows some failure in predicting the ground state and magnetic properties [1]. Recently, Perdew and Wang (PW) proposed a correction to the local spin density approximation (LSDA) considering an exchange-correlation functional, in terms of the electronic spin density and its gradient [2]. This correction is simple to apply in selfconsistent calculations in atoms, molecules, solids and leads to an improvement for some ground state properties.

Here, we compare the LSDA to the PW potential by analyzing the stability of differents ferromagnetic (FM) phases with respect to the non-magnetic (NM) phases for bcc and fcc iron, fcc nickel and fcc Ni-Fe alloys near the Invar region. All total energy calculations have been performed using the self-consistent LMTO method [3]. The calculations are semirelativistic and the core states are recalculated in each iteration.

In iron, the LSDA calculated fcc NM phase is found to be more stable than the bcc FM phase, contrary to the experiment. This calculation was performed with the parametrization of Vosko, Wilk and Nusair (VWN). The PW correction stabilizes the FM phase, increases its equilibrium volume and reduces the bulk modulus [4], [5]. For the bcc ground state the value of the calculated lattice constant is 5.4 a.u. and the bulk has a value of 1.7 Mbar compared respectively to the experimental values of 5.47 a.u. and 1.72 Mbar. The magnetic moment (for $a = 5.47$ a.u.) is 2.30 μ_B for PW, compared with 2.26 μ_B in the LSDA and 2.12 μ_B from the experiment.

	Fe (bcc FM - fcc NM)		**Ni** (fcc FM - fcc NM)		**Fe_3Ni** (fcc FM - fcc NM)	
	LSDA	PW	LSDA	PW	LSDA	PW
ΔE (mRy)	2.1	-13.4	-2.8	-3.6	-0.5	-13.0
ΔV (a.u.^{3})	5.59	8.43	0.60	0.67	3.1	7.99
p (Mbar)	-0.05	0.23	0.69	0.79	0.02	0.24

In Fe-Ni system, at low temperature, the fcc phase is stable from pure Ni to Invar concentration (65% of Fe) while a transition fcc-bcc occurs near the iron rich region. These

Invar alloys are characterized by several anomalies (related to their small thermal expansion coefficient at room temperature) which seem to be connected with the existence of almost degenerate high and low spin magnetic configurations [6]. The PW potential corrects the LSDA overbinding and increases the energy difference ΔE between the minima of the NM and FM phase (as in iron) but this effect seems too large. Several experiments indicate that at low temperature, the critical pressure $p = -\Delta E/\Delta V$ necessary to induce a transition from a FM phase to a low magnetic phase is about 0.06 Mbar [7], which is smaller compared to the PW value. The volume difference ΔV between the minima of the two phases is increased with the PW correction.

In fcc Ni, the differences ΔV and ΔE are small both for the LSDA and the PW potential. The critical pressure p is slightly increased in the PW scheme. The magnetic moment for the PW and LSDA potential are almost equal (0.62 μ_B).

The PW corrections do not significantly modify band-structure properties except for the exchange splitting which increases (PW, LSDA, experimental values are respectively 2.5, 2.4, 1.2-2.0 eV in iron and 0.75, 0.7, 0.3-0.5 eV in nickel). In Fe_3Ni, the increased exchange splitting produces a large reduction of the density of states at the Fermi level.

In conclusion the LSDA overbinding is corrected and ferromagnetism is favored in the FM phase, which is wanted for iron but which is exagerated in Invar alloys. Since the typical Invar properties are associated with a small difference in total energy between NM and FM states they are good for testing new potentials. Our calculations show that the PW potential gives a too large difference in total energy. Excepted the increase of exchange splitting, band properties are not significantly changed. Moreover the calculated PW magnetic moments are too large and their variation with pressure are to small. A most carefully study of the correlation spin dependence is needed in the corrections to the LSDA in order to improve the description of magnetism in the 3d materials.

References

[1] N.E. Christensen, O. Gunnarsson, and O. Jepsen, J. Physique Coll. **49** C8, 17 (1988)

[2] J.P. Perdew and Y. Wang, Phys. Rev. B **33**, 8800 (1986); J.P. Perdew, Phys. Rev. B **33**, 8822 (1986); Phys. Rev. B **34**, 7406 (1986)

[3] O.K.Andersen, Phys. Rev. B **12**, 3060 (1975); G.Arbman and T.Jarlborg, J. Phys. F **7**, 1635 (1977)

[4] P. Bagno, O. Jepsen and O. Gunnarsson, Phys. Rev. B **40**,1997 (1989)

[5] B. Barbiellini, E.G. Moroni and T. Jarlborg, J. Phys. Condens. Matt. **2**, 7597 (1990)

[6] E.G. Moroni and T. Jarlborg, Phys. Rev. B **41**, 9600 (1990)

[7] M.M. Abd-Elmeguid, B. Schleede and H.Micklitz, J. Magn. Magn. Mat. **72**, 253 (1988)

High resolution photoemission in the URh_3B_x system.

J.M. Imer, D. Malterre, M. Grioni, P. Weibel, B. Dardel, and Y. Baer

Institut de Physique, Université de Neuchâtel, CH 2000 Neuchâtel
Switzerland

abstract : High resolution photoemission measurements have been carried out in the URh_3B_x alloys. In this system, a progressive localization of 5f electrons occurs with increasing boron content. Whereas band structure calculations predict a pronounced increase in the density of 5f states at the Fermi level between URh_3 and URh_3B, our photoemission experiments show that the 5f spectral function is nearly insensitive to the boron addition. Then, the description of 5f states in terms of one-electron band calculations is questionable.

Uranium compounds are known to exhibit a large variety of physical properties (superconductivity, magnetic order, Kondo effect) which seems to be connected to the itinerant or localized character of 5f electrons. We present here a high resolution photoemission study of the URh_3B_x alloys. In this system, specific heat and magnetic susceptibility data suggest a progressive localization of 5f electrons with increasing boron content: URh_3 exhibits a Pauli susceptibility with a small linear coefficient of the specific heat ($\gamma = 14$ mJ/mol.K^2) whereas URh_3B orders antiferromagnetically at 9.5K with a γ value of 120mJ/mol.K^2 [1]. To explain this behaviour, band calculations in the local density approximation predict a dehybridization and a large modification of the 5f density of states (D.O.S.) when boron is added to URh_3 [1], namely a strong increase in the D.O.S. at the Fermi level (about a factor 4).

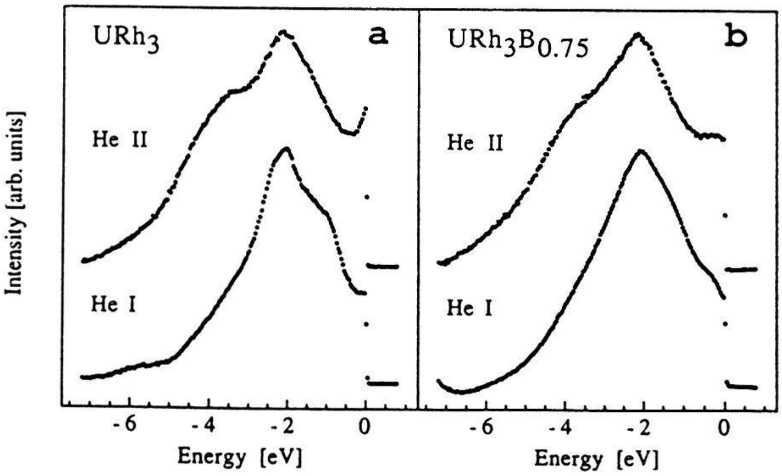

Figure 1:
a) UPS measurements of URh_3 for two photon energies.
b) idem for $URh_3B_{0.75}$.

These theoretical predictions are not consistent with our experimental spectra. Figure 1 shows HeI and HeII spectra (hν=21.2 eV and hν=40.8 eV respectively) of URh_3 and $URh_3B_{0.75}$. These spectra are dominated by a broad feature between -0.5eV and -6 eV which can be attributed to the rhodium 4d-derived band. Nevertheless, thanks to the large variation of 5f-cross sections with photon energy between 20 eV and 40 eV, the 5f spectral weight can be obtained by substracting the HeI spectra from the He II spectra. The differences, which are assumed to reflect the 5f states only, are plotted in figure 2. We can see that the 5f spectral weight exhibits a broad triangular peak culminating at E_F and extending over approximately 1eV in both samples. The 5f D.O.S. at the Fermi energy does not strongly increase with boron concentration as predicted by the band calculation; on the contrary, we observe an intensity decrease and a slight broadening. Then, the 5f spectral function appears to be quite insensitive to the changes in hybridization and 5f localization and interpretation of these 5f photoemission spectra in terms of single-particle density of states obtained from band calculation seems to be not relevant. In a recent work, we show that models used in high correlated systems like cerium compounds are more appropriate to describe these spectroscopic results [2].

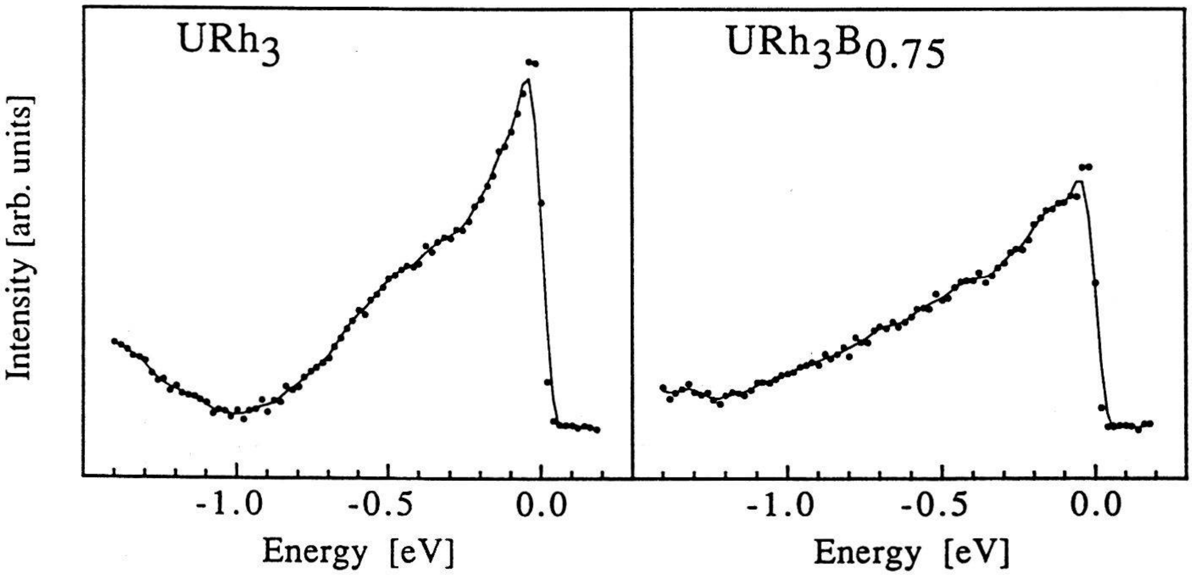

Figure 2: 5f spectral weight determined by the differences between HeI and HeII spectra for the two samples. The line is a guide for the eyes.

References

1 B.D. Dunlap, G.W. Crabtree, J.D. Jorgensen, H.A. Kierstead, D.D. Koelling, W.K. Kwok, D.J. Lam, S.K. Malik, A.W. Mitchell and S.C. Strite, Phys. Rev. B 39, 5640 (1989).

2 J.M. Imer, D. Malterre, M. Grioni, P. Weibel, B. Dardel, Y. Baer and B. Delley, submitted for publication in Phys. Rev. B.

ELECTRO-OPTIC PROPERTIES OF 4-(N,N-DIMETHYLAMINO)-3-ACETAMIDONITROBENZENE (DAN) BULK CRYSTALS AND FREQUENCY DOUBLING IN SINGLE CRYSTAL CORED FIBERS

P. Kerkoc and P. Günter
Institute of Quantum Electronics, Swiss Federal Institute of Technology
ETH-Hönggerberg, CH-8093, Switzerland

The dispersion of the linear electro-optic coefficients of DAN bulk crystals was measured. We used high quality samples prepared in our laboratory. The obtained values at the He-Ne laser wavelength (λ = 633 nm) are r_{22} = (12 ± 1) pm/V, r_{32} = (13 ± 2) pm/V, r_{12}= (4.0 ± 0.5) pm/V and r_{52} = (- 0.7 ± 0.2) pm/V. Near to the blue transparency cut-off at λ = 496.5 nm the largest linear electro-optic coefficient reaches a value of r_{32} = (36 ± 4) pm/V and a half-wave voltage $U_{\pi y}^{(z)}$ = (1.2 ± 0.4) kV. For DAN single crystal cored fibers 4 - 5 mm in length and of a diameter 4 - 5 µm, second-harmonic conversion efficiencies were achieved of up to 25% for doubling the 1064 nm line of a pulsed Nd:YAG laser with a fundamental peak power of 7.5 W.

The molecular crystal 4-(N, N-dimethylamino)-3-acetamidonitrobenzene (DAN) is very attractive for nonlinear optical applications due to its large nonlinear-optical susceptibility coefficient d_{23} = 50 pm/V [1]. Another second-order nonlinear optical effect, the linear electro-optic Pockels effect, is the topic of this investigation. Since only the (001) crystal face of monoclinic DAN crystals (point group symmetry 2) [2] can be polished with a high optical quality, the following procedure was developed for the measurement of linear electro-optic coefficients. Silver electrodes were deposited on the (010) crystal faces and an electric field was applied parallel to the y- axis of the principal dielectric system. The orientation of the principal dielectric system (x, y, z) relative to the geometry of a DAN crystal is given in ref. [1]. For this configuration the linear electro-optic coefficients r_{22}, r_{32}, r_{12} and r_{52} are accessible. For the measurement of the electro-optic coefficients the sample was set on a rotating stage and rotated around the y- axis. Two different polarizations of the beam, parallel to the y- axis or the x - z plane of the principal dielectric system were selected by a polarizer. The mounted crystal was placed in an arm of a Michelson interferometer for the measurement of the field induced phase retardation, as described elsewhere [3]. For the polarization of the beam parallel to the y- axis the r_{22} could be obtained directly. For the evaluation of the electro-optic coefficients r_{12}, r_{32} and r_{52}, the beam was polarized parallel to the x - z plane and the crystal was rotated clockwise and counter - clockwise around the y- axis. For every incidence angle δ of the light beam, the effective linear electro-optic coefficient r_{eff} was measured. The individual coefficients were then obtained by fitting the data to:

$$r_{eff} = r_{32} \cos^2\delta + r_{12} \sin^2\delta + r_{52} \sin 2\delta \,. \qquad (1)$$

The procedure was repeated at several wavelengths (two Ar^+, He-Ne, Rhodamine 6G dye) and the obtained linear electro-optic coefficients r_{m2} (m = 1, 2, 3, 5) with the corresponding reduced half-wave voltages $U_{\pi y}^{(1)}$ are listed in Table I.

Table I. Linear electro-optic coefficients r_{m2} (m = 1, 2, 3, 5) and the corresponding reduced half-wave voltages $U_{\pi y}^{(l)} = \lambda / \left(n_l^3 r_{m2}\right)$ of DAN crystals for light propagation along the axes of the principal dielectric system (l = x, y, z) at different wavelengths of laser light.

λ (nm)	r_{22}[pm/V]	r_{32}[pm/V]	r_{12}[pm/V]	r_{52}[pm/V]	$U_{\pi y}^{(y)}$ (kV)	$U_{\pi y}^{(z)}$ (kV)	$U_{\pi y}^{(x)}$ (kV)
632.8	12 ± 1	13 ± 2	4.0 ± 0.5	-0.7 ± 0.2	12 ± 4	8 ± 4	36 ± 10
585.5	14 ± 1	15 ± 2	5 ± 1	-1.0 ± 0.3	10 ± 2	6 ± 2	32 ± 6
514.5	22 ± 2	25 ± 3	7.3 ±1.5	-1.5 ± 0.4	4 ± 1	2 ± 1	18 ± 4
496.5	32 ± 2	36 ± 4	8.0 ± 2	-2.1 ± 0.6	2.0 ± 0.6	1.2 ± 0.4	14 ± 2

The linear electro-optic coefficients of DAN measured in our experiments at a modulation frequency of 1 kHz are about a magnitude lower than that potassium niobate with the $r_{42} = 380$ pm/V at the wavelength $\lambda = 633$ nm [4]. But they are expected to be larger than the ones found in most inorganic ferroelectric crystals at high modulation frequencies ($\approx$ 1 GHz), where lattice vibrations are clamped and the electronic contributions dominate.

Second-harmonic generation (SHG) experiments were performed on DAN single crystal cored fibers of 4 - 5 mm length and 4 - 5 µm in diameter. As laser sources we used an Nd:YAG pumped optic parametric oscillator (OPO) and a pulsed Nd:YAG laser (BMI 501 DNS). It was observed that DAN fibers were phase-matchable for the whole spectral range (960 - 1200 nm) achievable with the existing OPO for the propagation direction of the fundamental beam along their growth crystallographic a- [100] axis. For fundamental beams composed of the idler $I^{(\omega_1)}$ and signal $S^{(\omega_2)}$ waves in the spectral range of 1100 - 1000 nm of the OPO, a total conversion efficiency of 10% was measured for a fundamental peak power of 7.5 W. Besides frequency doubling $\left(I^{(\omega_1)} \rightarrow I^{(2\omega_1)}\right)$ and $\left(S^{(\omega_2)} \rightarrow S^{(2\omega_2)}\right)$ also a phase-matched sum frequency $\left(I^{(\omega_1)} + S^{(\omega_2)}\right) \rightarrow (S+I)^{(\omega_1+\omega_2)}$ was generated. The SHG experiments with the Nd:YAG laser ($\lambda = 1064$ nm) gave conversion efficiencies up to 25% for the same fundamental power. The discrepancy between the conversion efficiencies can be accounted to the relatively wide spectral width of the OPO (20 - 30 nm) which is much larger then the acceptance band width of $\Delta\lambda = 0.12$ nm at the dispersion parameter $D^{(\omega)} = 0.53$ for a crystal thickness d = 4 mm as compared to the spectral width of 0.07 nm observed in the Nd:YAG laser.

This work was supported in part by the Swiss National Foundation (NFP 19: Materials for Future Technology).

References

[1] P. Kerkoc, M. Zgonik, K. Sutter, Ch. Bosshard and P. Günter, J. Opt. Soc. Am. B **7**, 319 (1990).

[2] R.J. Twieg and C. W. Dirk, Res. Rep. RJ 5329 (54799) (IBM Alm. Res. Cent., San Jose, Calif., Oct. 1986).

[3] K. Sutter, Ch. Bosshard, M. Ehrensperger, P. Günter and R.J. Twieg, IEEE J. Quant. Electr. **24**, 2362 (1988).

[4] P. Günter, Opt. Comm. **11**, 285 (1974).

High-field magnetoconductivity of electrons on liquid helium

P. Scheuzger, J. Neuenschwander, and P. Wyder
Max-Planck-Institut für Festkörperforschung, Hochfeld-Magnetlabor, BP 166X,
F-38042 Grenoble Cedex, France

We have measured the longitudinal magnetoconductivity σ_{xx} of a nondegenerate two-dimensional gas of electrons on a liquid helium surface in high magnetic fields. At strong fields, deviations from the classical parabolic behaviour are observed. We compare our results with a quantum transport theory of short-range scattering within broadened Landau levels.

Electrons deposited on the surface of liquid helium form one of the simplest and most ideal two-dimensional electron systems. At all practical temperatures, the Fermi energy $E_F \ll kT$, so that we deal with a nondegenerate two-dimensional electron gas (2DEG). For temperatures above 1 K , the scattering is completely determined by collisions between electrons and vapor atoms. In the presence of a strong magnetic field perpendicular to the layer, the motion of the electrons is restricted to Landau orbits and the energy spectrum becomes discrete. To calculate the electron transport in this case, a quantum mechanical description is required.

The main purpose of the present work is to explore the magnetoconductivity of electrons on helium in the extreme quantum limit. Measurements were performed for temperatures of $T = 1.5 - 2K$ and magnetic fields up to 22T.

To investigate the conductance of the electrons on helium we used the Sommer-Tanner technique [1] in an experimental cell with a Corbino geometry [2]. Electrons were deposited on the helium surface by pulse-heating of a tungsten filament. We measured the complex impedance presented by the Corbino geometry with a capacitance-conductance bridge in conjunction with a dual-phase lock-in amplifier. From this the conductance of the 2DEG was determined using a simplified equivalent circuit analysis [2]. The electron density n_e was calculated from the vertical holding field and was of the order of $n_e = 10^7 - 10^8 cm^{-2}$.

At fields $B > 10T$ we observed a deformation of the helium surface due to the diamagnetism of ^{4}He and radial field gradients. Minimizing the sum of gravitational and magnetic energy we calculated the shape of the surface. The deformation causes a redistribution of the electrons, i.e. $n_e = n_e(r, B)$ (r: distance from the center). Since $\sigma_{xx} \propto n_e$ we can correct the measurements for this effect.

At low magnetic fields we observe classical magnetoconductivity as described by the Drude model. For higher magnetic fields the system enters the quantum limit, i.e. $\hbar\omega_c > kT$ (ω_c: cyclotron frequency) and the curves show a reduced field dependence. High field magnetoconductivity is governed by intra Landau level scattering. In the presence of impurities, the Landau levels are broadened. Neglecting scattering by clusters of impurities, Ando and Uemura get a semi-elliptic DOS [3]. Including multiple-scattering processes, Ando [4] and also Gerhardts [5] get a gaussian DOS (for δ-like impurities). From these DOS combined with Boltzmann statistics, $\sigma_{xx}(B)$ can be calculated analytically. For a semi-elliptic DOS we get

$$\sigma_{xx}(B) = \frac{2\coth(\hbar\omega_c/2kT)}{\pi\, I_1(\Gamma/kT)} \left(\cosh\left(\frac{\Gamma}{kT}\right) - \frac{kT}{\Gamma}\sinh\left(\frac{\Gamma}{kT}\right)\right)\frac{n_e e}{B}$$

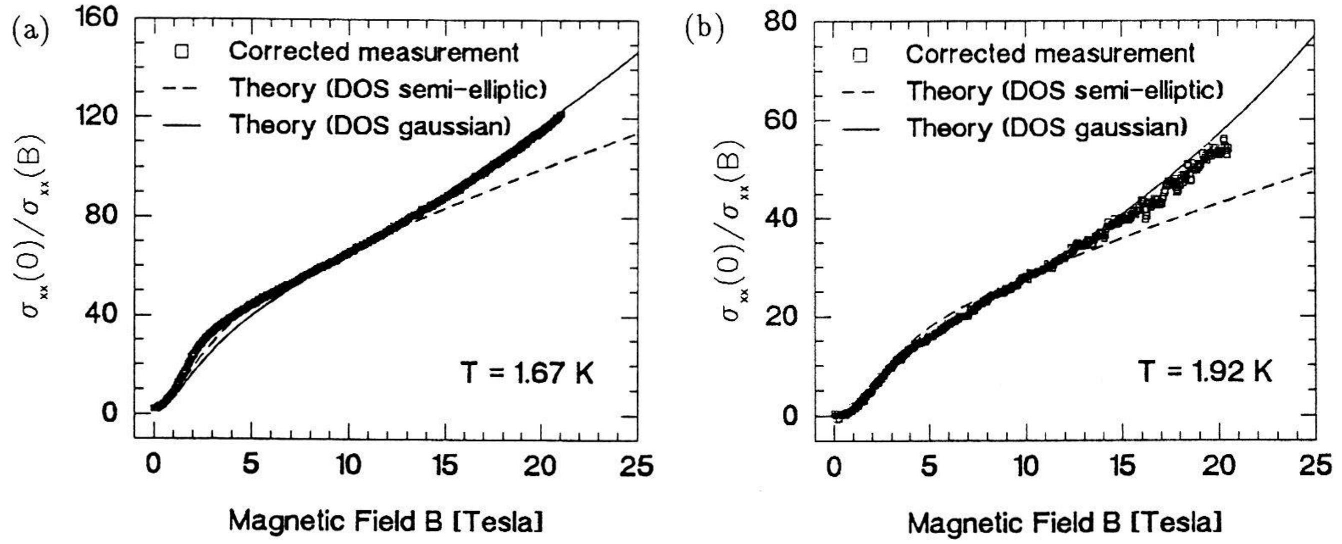

FIG. 1. Inverse magnetoconductivity of electrons on liquid helium. Helium height h at $B = 0T$ is (a) $h = 0.49mm$, $n_e = 1.2 \times 10^8 cm^{-2}$, (b) $h = 1.04mm$, $n_e = 5.6 \times 10^7 cm^{-2}$

For gaussian DOS we get

$$\sigma_{xx}(B) = \frac{\sqrt{\pi}}{4}\frac{\Gamma}{kT}\exp\left(-\left(\frac{\Gamma}{4kT}\right)^2\right)\coth\left(\frac{\hbar\omega_c}{2kT}\right)\frac{n_e e}{B} \qquad \text{where } \Gamma = \frac{\hbar e}{m}\sqrt{\frac{2B}{\pi\mu_0}}$$

is the half-width of the Landau level. I_1 is the modified Bessel function of order 1 and μ_0 is the zero-field mobility. In Fig.1 $\sigma_{xx}(0) = n_e e \mu_0$ was calculated with values for μ_0 according to [6]. To get rid of a geometrical factor and also to be independent of the electron density n_e, we plot the ratio $\sigma_{xx}(0)/\sigma_{xx}(B)$. We normalized our data and also the theoretical curve for semi-elliptic DOS to the value of the theoretical curve for gaussian DOS at 10T. Assuming an experimental linewidth $\Gamma_{exp} = 2\Gamma_{theor}$ as reported in [2] we get good qualitative agreement between our high-field data and the theoretical calculations for gaussian DOS.

In conclusion, we have measured the high-field magnetoconductance of electrons on liquid helium. Our data can be fitted by theoretical calculations which assume a gaussian DOS. The experimental linewidth Γ_{exp} resulting from this fit is larger then the value predicted by the theory.

We wish to thank R. van der Heijden and A. Janssen for communicating much advice on their experimental techniques. We are grateful for contributions from W. Joss, J.C. Maan and G. Maret.

References

[1] W.T. Sommer and D.J. Tanner, Phys.Rev.Lett. **27** (1971) 1345.

[2] R.W. van der Heijden et al., Europhys.Lett. **6** (1988) 75.

[3] T. Ando and Y. Uemura, J.Phys.Soc.Jpn. **36** (1974) 959.

[4] T. Ando, J.Phys.Soc.Jpn. **37** (1974) 622.

[5] R.R. Gerhardts, Surf.Sci. **58** (1976) 227.

[6] M. Saitoh, J.Phys.Soc.Jpn. **42** (1977) 201. (1972) 859.

Tentative Cellular Automaton model for a Solid-Liquid-Gas system on a hexagonal lattice

D.G. Maeder
Section de Physique, DPNC
Université de Genève, CH 1211

Moving particles of ideal gases are represented by the 6 low bits (#0..5) of the cell state using C.A.rules of the well-known FHP model[1]. An extended version using an additional bit (#6) to represent particles at rest assumes creation or annihilation of such "cold" particles with equal probability whenever the respective collisions conserve the momentum. One might be tempted to define an effective temperature derived from the ratio of total numbers of "hot"(i.e. moving) to "cold" particles in the system. We have made computer runs on a 100×100 cell FHP model in which the "cold" particle annihilation (or creation) probabilities were set proportional to a Boltzmann factor $\exp(-\beta)$ (or its complement resp.) by a random generator, and observed satisfactory agreement with the expected relation $T_{\text{eff}} \times \beta = \text{const.}$

Other extensions of the FHP model are being studied for representing deviations from ideal gas behaviour. Very recently, Chen et al.[2] have described a model where head-on collisions between gas particles may result in the creation of "bound pairs" that can be interpreted as particles of a different phase, such as a liquid. Evaporation/condensation probabilities are governed by exponential functions, in a similar manner as indicated above except that exponents in the Boltzmann factor have to be multiplied by the number of bound pairs in the neighbourhood which all contribute to a cohesion force potential. In [2] however, no cold gas particles were considered; consequently the remaining gas always appears quite hot, even when most of its particles have wound up in the condensed phase.

Having experimented with the FHP model extended to the T_{eff} concept explained above, it seemed to us quite natural to attribute a cohesive force potential to all neighbouring particles at rest, and thus even to go one step further: using two additional bits (#6,7) for defining the cell state allows distinction of 3 different kinds of particles at rest, assigned to

- single gas particles(mass=1), or
- bound pairs (liquid, mass=2), and
- triplets (solid, mass=3).

The sum of all these masses at rest in the hexagonal neighbourhood (including the center cell) could - without any selective guiding restrictions - attain a maximum of $NR = 21$ units at very low temperatures. We have tentatively introduced a cohesive force increasing up to $NR = 4$, while for $NR > 14$ an increasing repulsion opposes the growth of an unstructured lump of coherent solid mass. A surface term rule favours the formation of droplets in the liquid phase, while triplet formation is subject to restriction rules that give the solid mass a dendritic-like appearance, with an average mass density close to the liquid one. At the present stage, the gas-liquid transition occurs around $\beta \approx 1.5$ while below $\beta \approx 4$ only gas and solid particles can coexist. A more detailed paper will be published elsewhere.

[1] Frisch U, Hasslacher B, and Pomeau Y, Phys.Rev.Lett. 56,1505(1986).
[2] Chen H, Chen S, Doolen GD, Lee YC, and Rose HA, Phys.Rev.A 40,2850(1989).

EVALUATION EXPERIMENTALE DU COURANT DE DESTRUCTION DE L'ETAT MIXTE A DEUX DIMENSIONS DANS LES COUCHES MINCES D'INDIUM

A. Cossy-Favre, E. Holguin, B. Dutoit et L. Rinderer

Institut de Physique Expérimentale de l'Université de Lausanne, CH-1015 Lausanne.

RESUME

Nous présentons une théorie macroscopique donnant la variation du courant de destruction (I_m) de l'état mixte à deux dimensions (M) en fonction de la température. Des expériences réalisées sur des couches cylindriques minces d'indium ayant une épaisseur de 5.1µm, montrent que les densités de courant nécessaires à la destruction de cet état peuvent atteindre 10^5 A/cm^2. Sur la base de ces mêmes expériences, la théorie permet de calculer l'épaisseur de l'état M qui serait de l'ordre de la longueur de cohérence.

1. INTRODUCTION

La destruction de la supraconductivité dans un cylindre creux de type I, par un courant surcritique $I > I_c$, provoque l'apparition de l'état mixte à deux dimensions (M) à la surface intérieure du cylindre [1]. Cet état possède une très faible résistivité et sa dimension est de l'ordre de la longueur de cohérence ξ [2]. Pour des échantillons très épais, il peut être détruit en appliquant un courant $I_m \approx r_2 I_c/2\xi$ [3], où r_2 est le rayon externe du cylindre.

Nous avons cherché à définir ce courant de destruction pour des couches minces d'indium dont l'épaisseur $\varepsilon \rightarrow \xi$.

2. PARTIE EXPERIMENTALE ET DISCUSSION DES RESULTATS

Les couches minces ont été évaporées sur des tiges de quartz de rayon r_1 dont une des extrémités était accrochée à l'essieu tournant d'un moteur. Afin d'atténuer les vibrations, une vitesse angulaire $\omega = 0.1\pi$ rad/s a été choisie.

Les caractéristiques courant-tension ont été mesurées en a.c. pour éviter au maximum l'échauffement des échantillons. Nous avons soumis l'échantillon à un courant formé d'impulsions carrées de 1ms de longueur générées à une fréquence de 1Hz .

A partir de la formule donnant I_m dans le cas des échantillons très épais, on calcule la densité de courant J_m nécessaire à détruire l'état M:

$$J_m \approx \frac{I_c}{2\pi r_2 \xi} \qquad (1)$$

Cette densité de courant peut être plus facilement atteinte dans les couches minces. Une étude préalable [4] faisant intervenir le rôle de l'état intermédiaire (L) dans ces couches, a permis d'établir que

$$\frac{I_l}{I_c} \approx 1 + \frac{(\varepsilon - \xi)^2}{2 r_1{}^2} \qquad (2)$$

où I_l est le courant de destruction de l'état L. Nous voyons que si $\varepsilon \rightarrow \xi$, alors $I_l \approx I_c$, et la densité de courant permettant l'élimination de l'état M dans l'échantillon est celle donnée par la relation (1).

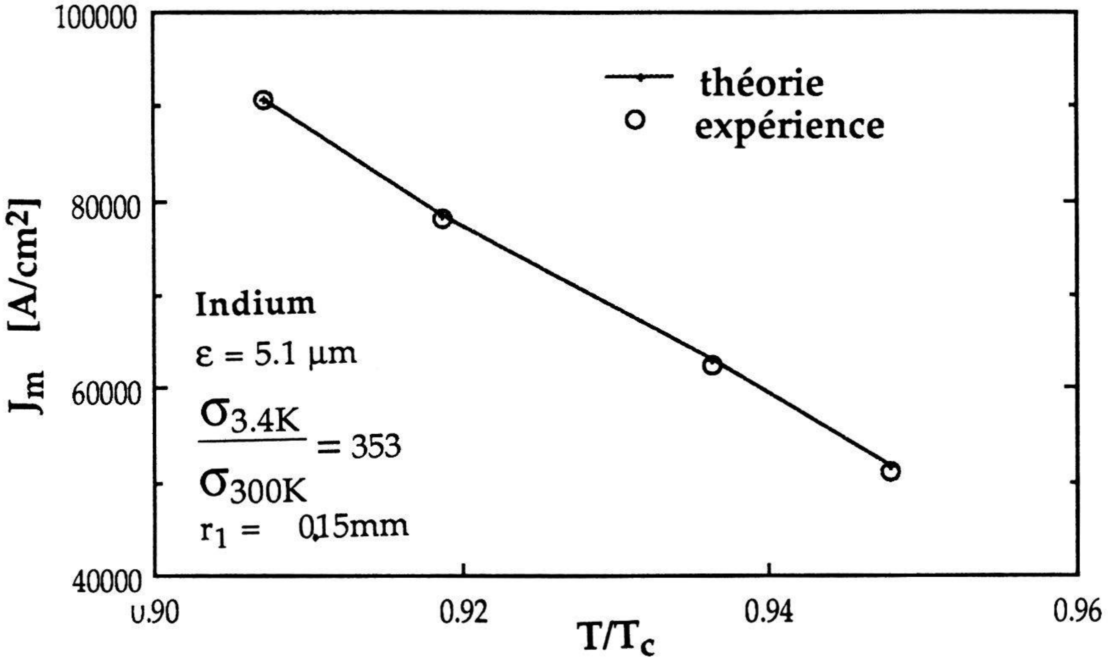

Fig.1
Densité de courant de destruction de l'état mixte à deux dimensions.

La Fig.1 montre des résultats obtenus sur une couche d'indium de 5.1μm d'épaisseur. Elle représente la variation de J_m en fonction de la température réduite T/T_c dans un domaine de température. Les valeurs expérimentales de l'épaisseur de l'état M peuvent être calculées d'après [3] en mesurant la pente $m = \varepsilon/(\varepsilon - \xi)$ de la caractéristique, lorsque $I_l < I < I_m$. L'épaisseur de l'état M ainsi déterminée peut convenablement se mettre sous la forme $\alpha\xi$, où α (ici valant 1.6) est un facteur numérique dépendant essentiellement de l'état résistif de la couche.

3. CONCLUSION

Ces résultats permettent de dire que l'épaisseur de l'état M est de l'ordre de la longueur de cohérence et que la variation de J_m en fonction de T/T_c est conforme à la théorie.

REMERCIEMENTS

Nous adressons nos remerciements à G. Burri, R. Schöpfer, et J. Rittener pour leur aide sur le plan technique. Ce travail a été financé par Le Fonds National Suisse pour La Recherche Scientifique.

REFERENCES

[1] I.L. Landau and Yu. V. Sharvin, JEPT Lett. 10, 121 (1969).
[2] A.F. Andreev and P. Tekel, Sov. Phys. JEPT 35, 807 (1972).
[3] E. Holguin and L. Rinderer, Helv. Phys. Acta 60, 827 (1987).
[4] A. Favre, E. Holguin, B. Dutoit et L. Rinderer, Physica B, vol. 65 & 66, 1471 (1990).

ANOMALOUS FIELD DEPENDENCE OF CRITICAL CURRENT IN $Bi_2Sr_2CaCu_2O_{8+y}$ FILMS MADE BY THE LASER ABLATION

Takeshi Fukami*, Takashi Yamamoto**, Yuuji Yamasaki**
Kazuhiro Miyoshi** Yuuji Horie** and Leo Rinderer

Institute of Experimental Physics, University of Lausanne
CH-1015 Lausanne-Dorigny, Switzerland
(*On leave from Department of Physics, Kyushu University, Fukuoka 812)
**Department of Physics, Kyushu University, Fukuoka 812, Japan

Abstract : We have measured the field dependence of critical current as a parameter of temperature in $Bi_2Sr_2CaCu_2O_{8+y}$ films prepared by laser ablation technique. The field dependence had an abrupt change in a threshold field H_T which decreases as the temperature increases. The plots of H_T versus T may suggest a phase transition from rigid flux lattices to a flux-lattice melting state.

Recently, as one of the hopeful candidates for explanation of an abnormally broad resistive transition width in magnetic field [1-6], a transition from rigid magnetic flux lattices to a flux-lattice melting state has been researched. The flux-lattice melting has been also investigated theoretically taking into account the wavevector-dependent elastic moduli for flux lattices and the crystal anisotropy. In particular, Houghton et al.[7] estimated a phase diagram of the flux-lattice melting on the temperature T-magnetic field H plane. Our aims of the investigation are to confirm some clear sign of the phase transition on the field dependence of the critical current and to confirm a phase diagram on T-H plane expected by the theories.

Thin films with about 1 μm thick were deposited on single crystalline MgO(100) substrates by the laser ablation method using Ar-F gas excimer pulse laser[5]. The electrodes were fabricated by evaporating silver metal. The resistance measurements were carried out by traditional four probe method in magnetic fields up to 11 T.

Figure 1 shows the plots of log J_c versus log H as a parameter of temperatures. The data shown in Fig. 1 were obtained for H//c-axis under 2 μV criterion. In low field region, these plots had a similar behavior that J_c decreased linearly, but in high field region very different behaviors were observed depending on the temperature. At 10 K and 15 K, the dependences were almost linear over field region from 0.05 T to 11 T. But at higher temperatures than 20 K, the dependences became strong in high magnetic field region. In particular, the change became stronger at temperatures higher than 27.5 K. Here, let us define a threshold field as a crossing point of a straight slope in low field region and one in high field region in log J_c

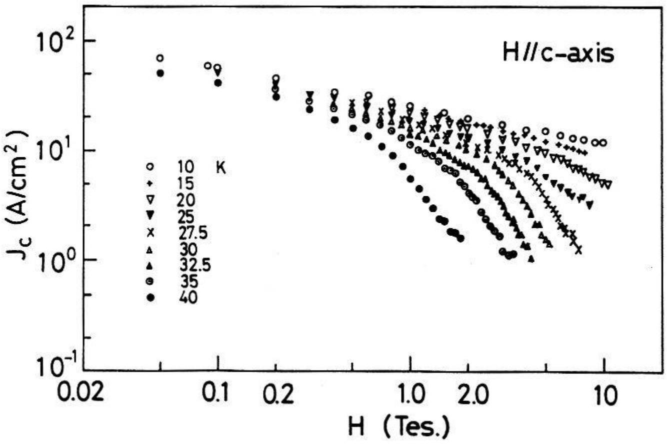

Fig. 1 Field dependence of J_c as a parameter of T for for H//c-axis.

versus log H curves. This point shifts to the weak field side as the temperature increases. For the case of H⊥c-axis, similar behaviors were observed, but at temperatures lower than 40 K the clear bending could be observed only for a few temperatures within 11 T. Using the values of H_T determined thus, plots of H_T versus T are shown in Fig. 2. For H//c-axis, these plots are limited within very narrow temperature region. The plots of the case of H⊥c-axis seem to shift to higher temperature side though only two points are obtained.

As was described in preceding paper, the weak J_c would originate from microbridges formed between superconducting grains, which work on as weak links for critical current. Since as-deposited films are in an amorphous state and they crystallize after an appropriate thermal processing, weak links may be formed between superconducting grains during this process.

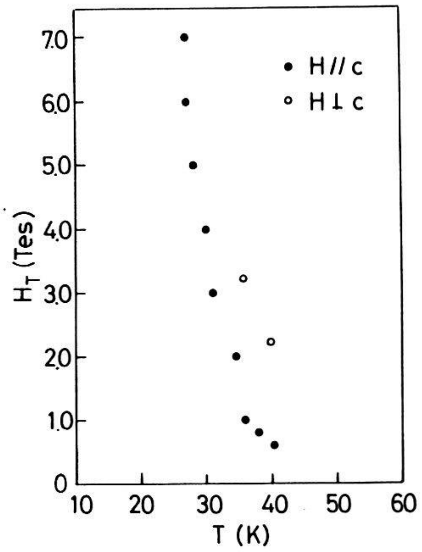

Fig. 2 Threshold field H_T versus temperature.

What is the origin of the abrupt change of the J_c versus H plots at high temperature region? One of the most hopeful candidates to explain the field dependence of J_c may be a transition from a rigid flux lattice to a flux-lattice melting state as the temperature increases. Gammel et al. used this concept to explain the mechanical properties in $YBa_2Cu_3O_7$ and $Bi_{2.2}Sr_2Ca_{0.8}Cu_2O_8$ in magnetic field [8]. They obtained a phase diagram on a T-H plane for this type of phase transition. This is very similar to one shown in Fig. 2. And this diagram is also very similar to one expected from the theoretical investigation by Houghton et al.[7]. Thus, abrupt change of J_c in J_c versus H plots as a parameter of T may be ascribed to the transition to the flux-lattice melting.

Acknowledgments

The authors wish to acknowledge valuable discussions with Prof. Takafumi Aomine and Prof. Bai-ru Zhao.

References

[1] T.T.M. Palstra, B. Batlogg, L.F. Schneemeyer and J.V.Waszczak, Phys. Rev. Lett. 61 (1988) 1662.

[2] H. Hidaka, M. Oda, M. Suzuki, A. Katsui, T. Murakami, N. Kobayashi and Y. Muto, Physica 148B (1987) 329.

[3] Y. Iye, T. Tamegai, H. Takeya and H. Takei, Jpn. J. Appl. Phys. 26 (1987) L1057.

[4] K. Kitazawa, S. Kambe, M. Naito, I. Tanaka and H. Kojima: Jpn. J. Appl. Phys. 28 (1989) L555.

[5] T. Fukami, T. Kamura, A.A.A. Youssef, Y. Horie and S. Mase, Physica C 159(1989) 422.

[6] T. Fukami, T. Kamura, A. A. A. Youssef, Y. Horie and S. Mase: Physica C 159(1989) 427.

[7] A. Houghton, R. A. Pelcovits and A. Sudbo, Phys. Rev. B 40 (1989) 6763.

[8] P. L. Gammel, L. F. Scneemeyer, J. V. Waszczak and D. J. Bishop, Phys. Rev. Lett. 61 (1988) 1666.

A HYSTERESIS OF MAGNETIC FIELD DEPENDENCE OF CRITICAL CURRENT IN $Bi_2Sr_2CaCu_2O_{8+y}$ FILMS PREPARED BY LASER ABLATION

Takeshi Fukami*, Terukazu Nishizaki**, Takashi Yamamoto***,
Takafumi Aomine*** and Leo Rinderer

Institute of experimental Physics, University of Lausanne
CH-1015 Lausanne-Dorigny, Switzerland
(* On leave from Department of Physics, Kyushu University, Fukuoka 812, Japan)
** Department of Information Systems, Kyushu University, Kasuga 816, Japan
***Department of Physics, Kyushu University, Fukuoka 812, Japan

Abstract : We measured the magnetic field H dependence of critical current I_c in $Bi_2Sr_2CaCu_2O_{8+y}$ (BSCC) films with c-axis orientation as a function of temperature T. A hysteresis of I_c versus H observed at the low temperatures became weaker as T increased and vanished at about 68 K. This hysteresis comes from the non-reversibility of I_c due to the pinning for the fluxoid in the bridge in the BSCC films.

Oxide superconductors have exhibited a pronounced broadening of the resistivity versus temperature T curves in the magnetic field H [1-4]. This broadening has been also observed not only under **I⊥H** but also under **I//H** [[2,4], here **I** is current vector and **H** magnetic field vector. This result shows that the macroscopic Lorentz force does not play any important role for the broadening. Therefore, we have examined whether the broadening is associated with the existence of bridges which work as weak links for I_c. One of the methods to certify the existence of bridges is to observe a hysteresis on the critical current I_c versus H when magnetic field is increases and decreases, because this hysteresis is originated from the existence of bridges as weak links [5-6].

The thin films were deposited on single crystalline MgO(100) substrates by the laser ablation technique using Ar-F excimer pulse laser [3] The c-axis of crystal almost orients perpendicular to the surface of the substrate. A zero resistivity temperature was 78.0 K. The I_c was measured by the same method as in previous works [5-9]. The I_c was taken to be the current at which the sample voltage reached 3μV.

Figure 1 shows typical H dependences of I at five temperatures for **H**//c-axis and Fig. 2 shows typical H dependences of I_c at three points of temperature for **H**⊥c-axis. The characteristic behaviors are summarized as follows. (1) A hysteresis is observed for **H**//c-axis, becomes weaker as the temperature increases and disappears at about 68 K. It can not be, however, observed for **H**⊥c-axis between 4. 2K and 78 K for **I⊥H** (2) The field dependence of I_c for **H**⊥c-axis is weaker than one for **H**//c-axis. (3) The noisy signals on the I_c at low temperatures become weaker as the temperature increases.

The SEM photograph in the previous work [3] shows that BSCC films on MgO substrate at room temperature prepared by the laser ablation technique consisted of irregular crystalline grains and pores. In addition to the above fact, the current density J_c was small compared with the values of J_c in refs. 10 and 11; J_c =8x10^4 A/cm^2 at 77 K and J_c = 10^5 A/cm^2 at 61 K, respectively. Then, the J_c of the films prepared by the laser ablation method would be determined by such a weak link as a bridge.

It has been shown that the hysteresis of Jc of superconducting granular aluminum bridges prepared by photolithography in low values of H, disappears as the temperature increases [6]. Furthermore, the I_c versus H curve in the Nb constant thickness bridge did not show any hysteresis for **I**//**H**, but when the **H** inclined only by 4 degrees from **I**, the clear hysteresis appeared [8]. And the cases for hysteresis to

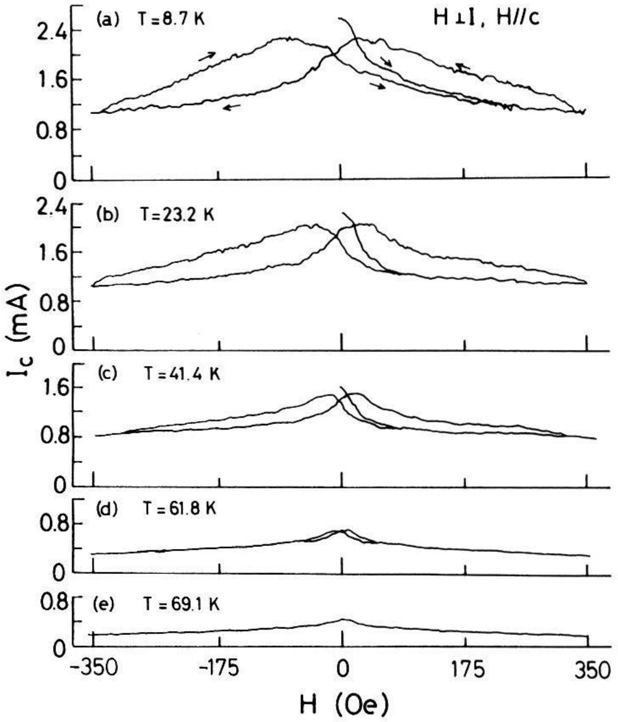

Fig. 1 Magnetic field dependence of I_c for **H**//c-axis.

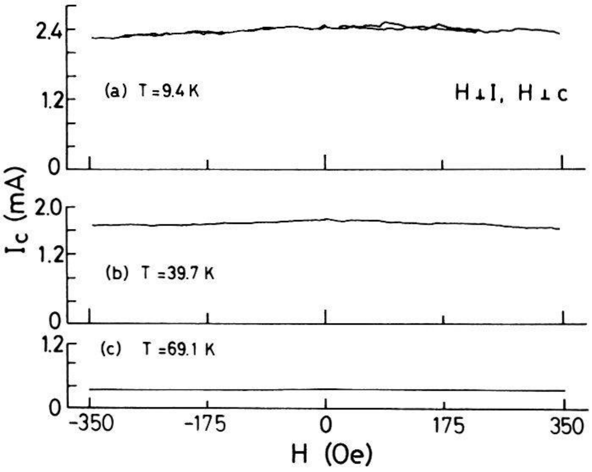

Fig. 2 Field dependence of I_c for **H**⊥c-axis.

disappear are in the following: the constricted part is too long for the electrical influence of the wide part adjacent to the constricted one to reach or the bulk pinning is dominant over the edge pinning. As for our films, for **H**//c-axis appropriately constricted part of bridge would exist also in films and they would enter a state in which at least one of the conditions mentioned above would realize effectively as the temperature increases. For **H**⊥c-axis, the bulk pinning may be dominant over the edge pinning [9]. The anisotropic behaviors of I_c versus H would be ascribed to the anisotropy of pinning force at bridges as weak links because of the preferred orientation of c-axis of the film.

References

[1] T.T.M. Palstra, B. Batlogg, L.F. Schneemeyer and J.V.Waszczak: Phys. Rev. Lett. 61 ((1988) 1662.
[2] K. Kitazawa, S. Kambe, M. Naito, I. Tanaka and H. Kojima: Jpn. J. Appl. Phy. 288 (1989) L555.
[3] T. Fukami, T. Kamura, A.A.A. Youssef, Y. Horie and S. Mase: Physica C 159 (1989) 427..
[4] T. Fukami, T. Kamura, A.A.A. Youssef, Y. Horie and S. Mase: Physica C 160 (1989) 991.
[5] K. Mizuno and T. Aomine: J. Phys. Soc. Jpn. 52 (1983) 4311.
[6] T. Aomine and A. Yonekura: Phys. Lett. 114A (1986) 16.
[7] T. Aomine and K. Tsuru: Jpn. Appl. Phys. 26 (1987) L2013.
[8] T. Yamamoto and T. Aomine: Jpn. J. Appl. Phys 27 (1988) L1917.
[9] T. Aomine, E. Tanaka, S. Yamasaki, K. Tani and A. Yonekura: J. Low Tem. Phys. 74 (1989) 263..
[10] J. Steibeck, B. Y. Tsaur, A. C. Anderson and A. J. Strauss: Appl. Phys. Lett. 54 (1989) 466.
[11] M. Hong, J. Kwo and J. J-. Yeh: J. Cryst. Growth 91 (1989) 382.

110K Bi-SYSTEM FILMS PREPARED BY RF-MAGNETRON SPUTTERING WITH COMPOUND TARGET

S. NICOUD, H. NAKANO[1], D. ABUKAY[2], M. SUZUKI[3] ,B. DUTOIT and L. RINDERER

Institut de Physique Expérimentale, Université de Lausanne,
CH-1015 Lausanne, Switzerland
(On leave from Nagoya University, Nagoya 464-01, Japan[1], EGE University, 35100 Bornova-IZMIR Turkey[2], Saga University, Saga 840, Japan[3].)

Abstract: The high-Tc Bi-system films (T_c > 100 K) could be obtained by a conventional method. The films were rf-magnetron sputtered from a compound target which was prepared by the mixture of Bi_2O_3, CuO, $SrCO_3$, $CaCO_3$ and PbO powders. After annealing, the temperature dependences of the electrical resistivity and the critical current density were measured. These experimental results show that the films have metallic characteristics with T_c(onset) >110 K and T_c(zero) ~ 105 K and they have mainly 110 K phase with small quantity of 80 K phase.

1. INTRODUCTION

High T_c Bi-system [1] is very interesting with the critical temperature T_c value in the range of 110K. The multiphase nature and the complicated structure make difficult to obtain the high quality thin films. The sputtering method is one of the suitable methods to fabricate high T_c films[2,3]. The high T_c Bi-system films with T_c > 100K could be obtained by a conventional sputtering method with a compound target. The electrical properties were measured and were discussed in view of the annealing conditions.

2. EXPERIMENTAL RESULTS AND DISCUSSIONS

The films were deposited on the (100) face of single crystal MgO substrate by rf-magnetron sputtering with a compound target. The target was prepared by the mixture of Bi_2O_3, CuO, $SrCO_3$, $CaCO_3$ and PbO, where the composition were adjusted to Bi:Pb:Sr:Ca:Cu = 2:1:2:2:3. The target of 100 mmϕ x 5 mm was formed by only pressing with a weak pressure. The sputtering power, time, gas, pressure and substrate temperature were 100 W, 120 min, Ar, 0.1 mBar and 600 °C, respectively. The as deposited films had very high electrical resistivities which were more than 10 Ω•cm at room temperature and did not show any superconductivity. The films were annealed at 840 - 860°C in air for 0.5 or 1 hours. The samples were put in and out to the heated furnace as soon as possible and the temperature change is estimated to be higher than 100 °C/min.

The resistivity and the critical current were measured for mechanically patterned bridge (length: ≤1 mm, width: ≤0.5 mm, thickness: ~2 μm) by the 4-probe technique. The temperature T of the sample holder was controlled between 10 and 295 K in a closed-cycle refrigerator. The electrical resistivity ρ was determined by the gradient of the current-voltage (I-V) curves at $I = \pm 10$ μA at each stabilized temperature. The critical current density J_c was obtained from the value of I at V ~ 20 μV. All of these measurements were realized by the computer-controlled system with high stability and accuracy.

Figure 1 shows the T-ρ characteristics of the films annealed under various conditions, where the ρ values are normalized by the value at 295 K (E3-1: 6.0 mΩ•cm, E3-3: 10 mΩ•cm, E4-20: 4.7 mΩ•cm, E5-20: 17 mΩ•cm). The characteristics strongly depend on the annealing temperature as shown in Fig. 1. The sample E5-20 which was annealed at 855 °C for 1 hour has T_c(onset) >110 K and T_c(zero) ~ 105 K. The samples annealed at temperature lower than 850 K have lower values of T_c(zero) (for example E3-1: 72 K, E3-3: 90 K). The samples annealed at temperature higher than 860 K also have lower T_c(zero) (for example E5-20: 78 K) and have rough surfaces which sometimes seem to be meshes. Figure 2 shows the T-$d\rho/dT$ characteristics normalized by the value of ρ_{295K}/295K, where the line of $\rho \propto T$ must be the constant value of 1. The resistance drop of E4-20 starts from 135 K and the peak of $d\rho/dT$ is

115 K as shown in Fig. 2. It indicates that the superconducting fluctuation may start from 135 K and the main parts have the transition temperature of 115 K.

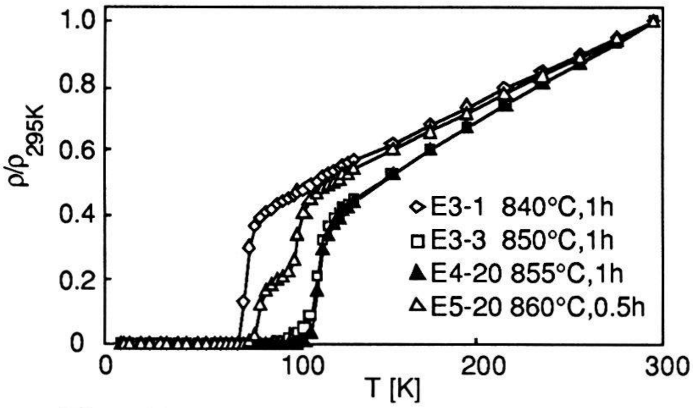

Fig.1 Temperature dependence of the electrical resistivities.

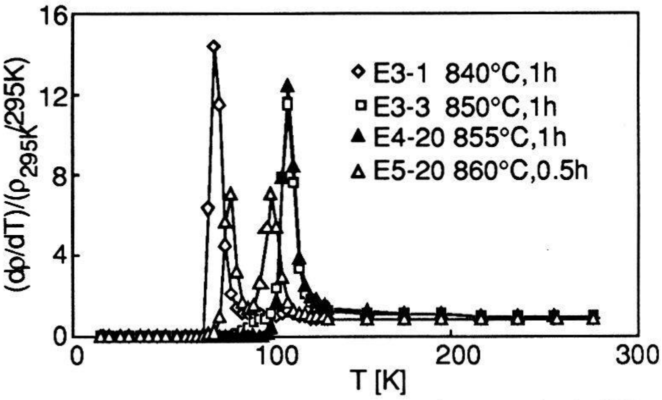

Fig.2 Temperature dependence of $d\rho/dT$ normalized by the value of $\rho_{295K}/295K$.

The samples E4-20, E4-s1 and E4-s2 annealed under the same condition show similar T-ρ characteristics. The T-J_c characteristics are shown in Fig. 3. The maximum value of J_c is about 10^4 A/cm^2 and these three samples has similar values and temperature dependance of J_c as shown in Fig. 2. The curves in Fig.3 slightly changed about at 80 K. The differential were calculated in order to emphasize the changes and the the value of dJ_c/dT clearly changed at 80 K as shown in Fig. 4. It indicates that the films contain the 80 K phase, but it seems to be not so large proportion as shown in Fig. 3.

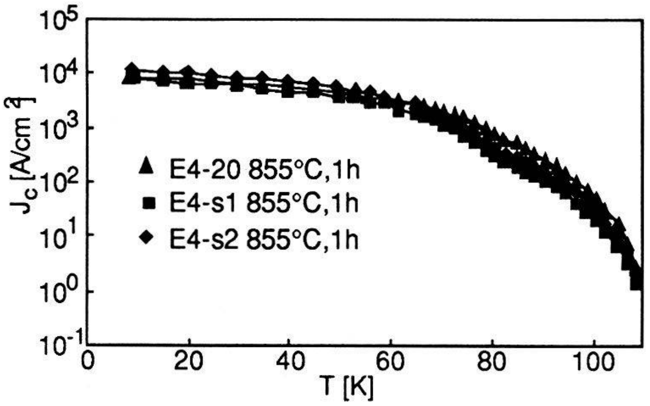

Fig.3 Temperature dependence of the critical currents

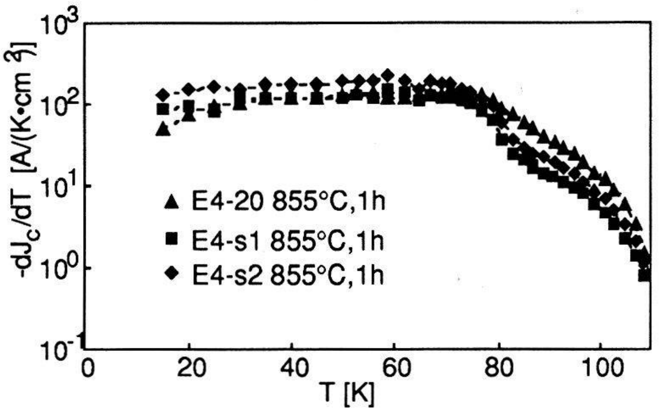

Fig.4 Temperature dependence of dJ_c/dT.

ACKNOWLEDGEMENTS

The authors thank Profs. Aomine and Fukami and Mr. Soares for their valuable suggestions and encouragement. They are also indebted to the Fonds National Suisse de la Recherche Scientifique.

REFERENCES

[1] H. Maeda, Y. Tanaka, M. Fukutomi and T. Asano, Jpn. J. Appl. Phys. 27, (1988) L209.

[2] Y. Kozono, T. Ohno, M. Kasai, M. Hanazono and Y. Sugita, Jpn. J. Appl. Phys. 28 (1989) L646.

[3] K. Ohbayashi, S. Suzuki, Y. Takai and H. Hayakawa, Proceeding of the 2nd International Symposium on Superconductivity (ISS89), Tsukuba, (1989) 841.

DYNAMICS OF FLUX PENETRATION IN SUPERCONDUCTING $(YBaCuO)_{1-x}Ag_x$ TUBULAR SAMPLES

E. HOLGUIN and H. BERGER
Institut de Physique appliquée, Ecole Polytechnique Fédérale, CH–1015 Lausanne
J.-F. LOUDE
Institut de Physique nucléaire, Université de Lausanne, CH–1015 Lausanne

Abstract

We describe the dynamics of flux penetration through the wall of superconducting, tubular $(YBaCuO)_{1-x}Ag_x$ samples, when an external magnetic field is suddenly applied. The flux penetration is characterized by a delay and a time constant which go through a maximum for $x = 0.3$.

1. Introduction

In previous papers [1, 2] we have investigated the dynamics of flux penetration in hollow YBaCuO samples when an overcritical magnetic field, produced by a coil surrounding the sample, is suddenly applied. This phenomenon is characterized by a delay Δt ($\cong 1\ \mu s$) and a time constant τ ($\cong 10\ \mu s$).

We already measured an $(YBaCuO)_{1-x}Ag_x$ sample with $x = 0.1$[3]; we here investigate the dependence of Δt and τ on x, at $T = 77$ K, for higher values of x, up to 0.5.

2. Experimental procedure and results

The ceramic samples ($x = 0.1$, 0.2, 0.3 and 0.5) were prepared by mixing appropriate quantities YBaCuO powder prepared in the standard way with Ag_2O. The mixture was ground and sintered, compacted into bars, and annealed for two days at temperatures between 900° C and 1040° C in oxygen. Subsequently, in the course of two days, the samples were cooled down to room temperature. In the next step, the samples were mechanically machined to their final tubular form (8–10 mm length, 4 mm outer diameter). With the addition of silver, the ceramic material becomes extremely hard; a diamond-tipped drill is required to bore the inner 2 mm hole.

The experimental setup has been published elsewhere [3]. A solenoid made of 20 unevenly spaced turns of wire generates in the sample volume a field which is uniform within ± 2%. An inner pickup coil measures the rate of variation of the magnetic flux in the center hole. We first determine the shielding magnetic fields H_{sh} and H_{shr}, respectively in single-shot and repetitive modes. H_{shr} is larger than H_{sh} when a magnetic flux is trapped in the sample.

If we suddenly apply an external magnetic field $H > H_{sh}$, the vortices first occupy a layer of thickness λ, on the external surface, and then diffuse into the whole sample due to their interacting forces. After a delay Δt, a front of vortices reach the inner wall and the pickup coil begins to sense a magnetic flux. Figure 1 shows a typical response $v(t)$ obtained with $x = 0.2$, when $B = \mu_0 H = 57.3$ G. The delay ($\cong 4\ \mu s$) can be precisely determined using the whole set of data. The experimental points are well fitted by a function of the form

$$y(t) \propto \mathbf{H}(t-\Delta t)\left[\exp\left(-\frac{t-\Delta t}{\tau_1}\right)-\exp\left(-\frac{t-\Delta t}{\tau_2}\right)\right] \tag{1}$$

where **H** is the Heaviside function, τ_1 ($\cong 35\ \mu s$) is the penetration time constant and τ_2 ($\cong 2\ \mu s$) is a much smaller time constant characterizing the finite rise time.

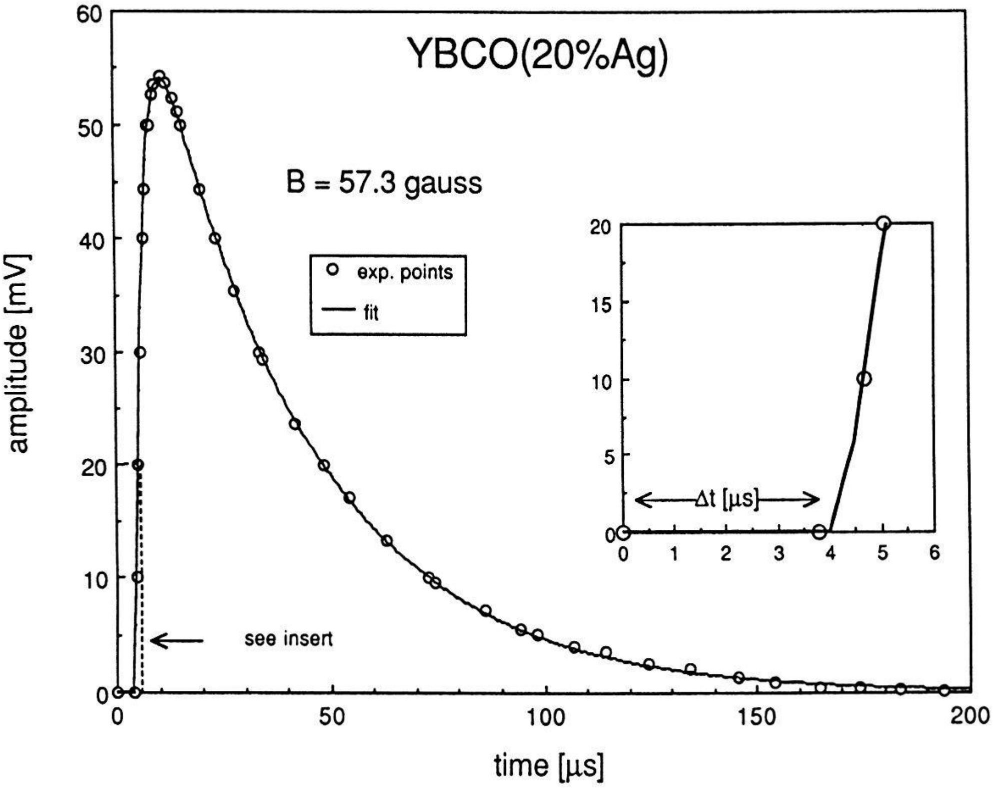

Figure 1.
Signal amplitude vs. time; $H/H_{sh} = 3.9$.
Insert: magnified region showing the time delay Δt.
Fit parameters:
$\Delta t = 4.28\ \mu s$
$\tau_1 = 35.4\ \mu s$
$\tau_2 = 2.24\ \mu s$

For $x = 0.1$, the values of Δt and τ_1 are close to their values for $x = 0$ [2].

For $x \geq 0.2$, the values of Δt and τ_1 are much larger than those observed in YBaCuO without silver [2]. The interstitial silver probably constitutes a source of pinning centers which delay the motion of the vortices. Δt is increased by about an order of magnitude; τ_1 is multiplied by a somewhat smaller factor. Both Δt and τ_1 are maximum for $x = 0.3$.

All samples show the same kind of dependence on the applied field H.

3. Conclusion

The dynamics of flux penetration in $(\mathrm{YBaCuO})_{1-x}\mathrm{Ag}_x$ is well characterized by a delay and a penetration time constant. These materials show a great environmental stability.

Acknowledgements

The authors are grateful for the technical assistance provided by Dr. H. J. Bühlmann (EPFL/IMO) and Mr. J. Knœpfli (EPFL/IPA). They wish to thank Dr. M. Jorand (UNIL/IPT) for many useful discussions and Prof. F. Lévy (EPFL/IPA) for his interest and support. This work was partially supported by the Swiss National Science Foundation.

References

[1] E. Holguin, H. Berger and J.F. Loude, Helv. Phys. Acta **63**, 507 (1990)
[2] E. Holguin, H. Berger and J.F. Loude, Solid State Commun. **74**, No 4, 263 (1990)
[3] E. Holguin, H. Berger and J.F. Loude, Physica B, **165&166**, 1391 (1990)

Spin - Polarization of the Electrons Thermoemitted from Fe and Ni

A. Vaterlaus, F. Milani, and F. Meier

Laboratorium für Festkörperphysik, ETH Hönggerberg, 8093 Zürich, Switzerland

Electrons thermoemitted from Fe and Ni at temperatures below the Curie temperature are unpolarized.

For a sample having a photothreshold of 1.4 eV and a temperature of 450 K a thermoemission current of 1 nA is expected [1] and observed. According to band structure calculations [2] a spin - polarization of -75 % and -4% is predicted for electrons 1.4 eV above the Fermi level in Fe and Ni respectively. However the measured polarization of the thermoelectrons is zero. The thermoemitted electrons loose their initial spin - polarization during the thermoemission process. In contrast, in photoemission the spin - polarization is conserved.

The samples were cylinders (5 mm diameter, 6mm long) of single crystalline Ni and high - purity polycrystalline iron. Standard surface preparation techniques were applied: Repeated cycles of Ar+ sputtering (1000 V) and annealing at 800 K. In order to lower the photothreshold a submonolayer of Cs was deposited onto the sample surface. In this way photothresholds of 1.4 ± 0.05 eV were obtained for both materials. It was found that the cesium stuck better to surfaces which were mildly sputtered before deposition. Then, even at the highest measuring temperature (450 K) no desorption of Cs took place ensuring a constant photothreshold. The spin - polarization P of the emitted electrons is measured by Mott scattering [3]. P is defined as $(N\uparrow - N\downarrow)/(N\uparrow + N\downarrow)$ where $N\uparrow(N\downarrow)$ is the number of electrons with spin magnetic moment parallel (antiparallel) to the surface normal.

Figure 1a shows the spin - polarization of the photoelectrons (full circles) and of the thermoelectrons (open circles) emitted from Ni(111) as function of the external field H. H is applied parallel to the surface normal. For thermoemission the sample is held at 449 K. The polarization of the thermoemitted electrons vanishes over the whole field range. Photoemission is performed at 406 K. For this temperature the thermocurrent becomes negligible compared to the photocurrent. As light source the 2.15 eV line of a HgXe lamp was used. The polarization of the photoelectrons does not vanish, therefore it is concluded that the sample is magnetic. It is saturated

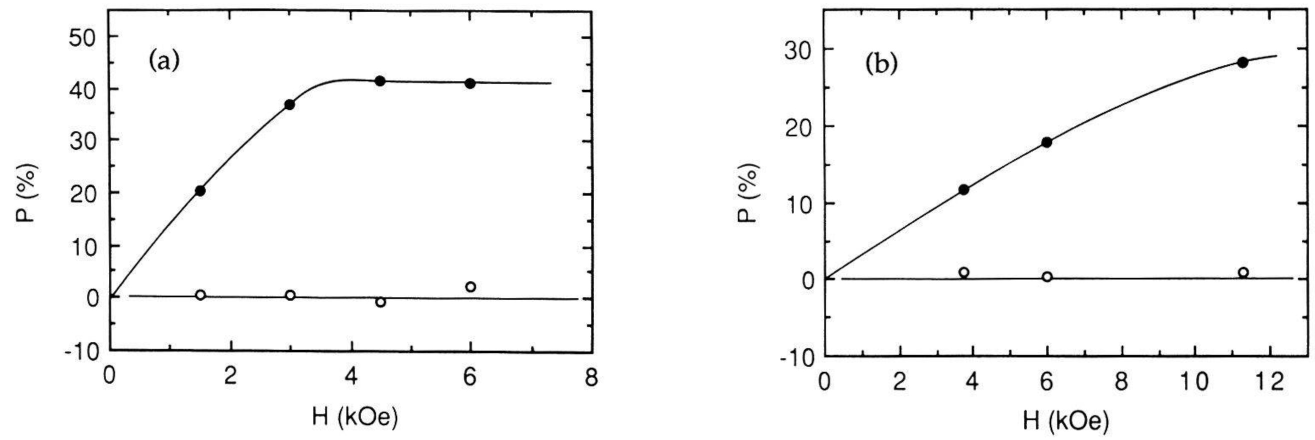

FIG. 1a Field dependence of the spin - polarization of the electrons thermoemitted (open circles, T = 449 K) and photoemitted (full circles, T = 406 K) from Ni (111). The work function is 1.37 eV. Photoemission is done with 2.15 eV light from a Hg - Xe lamp.

FIG. 1b. Open circles: Spin - polarization of the electrons thermoemitted from polycrystalline iron as function of the external field. The temperature is 423 K and the work function is 1.42 eV. Full circles: Superimposed to the unpolarized thermocurrent at 423 K is the photocurrent excited with 2.15 eV. Photocurrent and thermocurrent contribute an equal amount to the total electron yield.

along the surface normal for external fields exceeding 3.5 kOe.

The polarization of the electrons thermoemitted from iron is plotted in Figure 1b as function of the external field (open circles). The temperature of the sample is 423 K. The experimental outcome is the same as for Ni: P of the thermoemitted electrons vanishes. In order to probe the magnetic state of the sample it is exposed to 2.15 eV light from a HgXe lamp. The lamp intensity is adjusted such that the electron yield consists of an equal amount of thermocurrent and photocurrent. The polarization of the total electron yield is displayed by full circles in Figure 1b. P is different from zero due to the emission of polarized photoelectrons, which probe the magnetization along the surface normal of the sample [3].

The measurements displayed in Figure 1a and 1b show that the thermoemitted electrons carry no information about the magnetic state of the sample from which they are emitted. Their polarization is not accounted for by a single particle band structure.

References

[1] G. A. Haas, and R. E. Thomas, "Thermionic Emission and Work Function" in: Techniques of Metals Research Vol. VI (Edited by E. Passaglia), Interscience Publishers, 1972, p. 91 ff.

[2] H. Eckardt, and L. Fritsche, J. Phys. F: Met. Phys. 17, 925 (1987).
L. Fritsche, J. Noffke, and H. Eckardt, J. Phys. F: Met. 17, 943 (1987)

[3] M. Campagna, D. T. Pierce, F. Meier, K. Sattler. and H.C. Siegmann, Adv. Electron. Electron Phys. 41,113 (1976).

Sidebranching of Xenon Dendrites

E. Hürlimann, V. Peschak and J.H. Bilgram
Laboratorium für Festkörperphysik, ETH, 8093-Zürich

The sidearms of xenon dendrites growing into supercooled melt have been investigated for supercoolings $60\mathrm{mK} < \Delta T < 150\mathrm{mK}$. The spatial frequency and its coarsening has been determined. The sidearms grow on the top of the fins of the dendrite. The maximal amplitude w of the sidearms has been measured as a function of their position ℓ_p at the fin. We find $w \sim \ell_p^{1.72}$ independent of the supercooling.

The experimental setup is similar to the one described in [1]. The growth vessel (Fig. 1) immersed in a liquid bath is filled with about 80 ccm liquid xenon and cooled down to some mK below the triplepoint temperature. Crystal growth is initiated by the capillary injection technique. The dimensions of dendrites are small compared to the volume of the growth vessel. There are no confinement effects [2]. The dendrites are imaged by a self-built periscope at a CCD-camera with a resolution of about 8 µm. These highly contrasted pictures are digitized and the dimensions of the sidearms have been determined by computer and image processing.

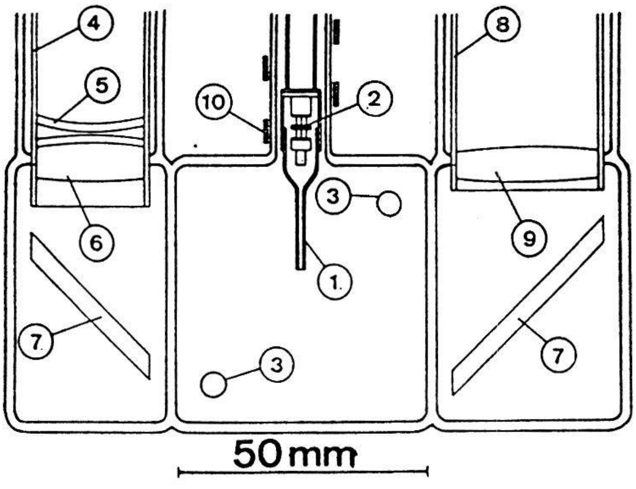

Fig.1 Growth vessel

1) capillary
2) Peltier element
3) temperature sensor
4) periscope
5) meniscus-lens
6) achromat
7) mirror
8) illumination system
9) lens
10) heater

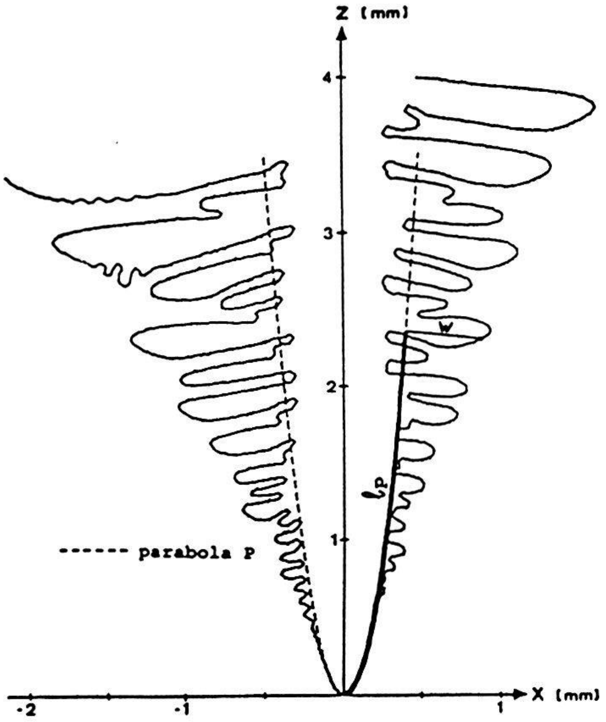

Fig.2 Contour of a xenon dendrite

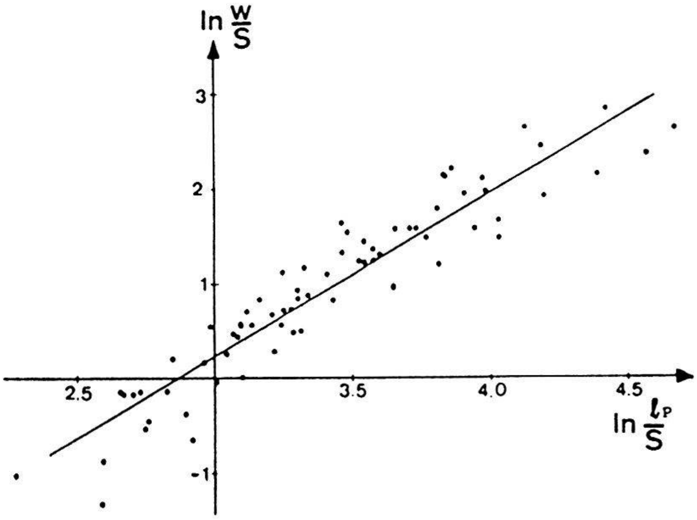

Fig.3 Amplitude w of the sidearms vs. the length ℓ_p of the parabola scaled with the sidearm spacing S

Fig. 2 shows a dendrite grown at $\Delta T = 150$ mK. The sidearms develop on top of the fins of the dendrite. The shape of the fins is fitted by the parabola P which is drawn to fit the shape of the dendrite tip. The amplitude of the sidearms on top of the fin is designated by w. In Fig. 3 w is plotted vs. the length ℓ_p of the parabola P. Dendrites of all ΔT are included. w and ℓ_p are scaled by the sidearm spacing S [1]. The spread of the points results from the inaccuracy of our parabola fit. The line which is drawn to guide the eye corresponds to $(w/S) \sim (\ell_p/S)^{1.72}$.

Acknowledgements: We thank Prof. H.R. Ott for his support. This work is supported by the Swiss National Science Foundation.

[1] J.H. Bilgram, M. Firmann and E. Hürlimann, J. Crystal Growth, 96, 175 (1989)
E. Hürlimann, R. Trittibach and J.H. Bilgram, Helv. Phys. Acta, 63, 473 (1990)

[2] R. Trivedi and J.T. Mason, Metall. Trans. (in press)

General Relations between the Restrictions Imposed by Different Point Groups on the Form of Property Tensors

H. Grimmer

Paul Scherrer Institut, 5232 Villigen PSI, Switzerland

If the form of a property tensor is known for those crystallographic point groups (CPGs) that consist of pure rotations only, it can immediately be given for any CPG. This is clear for tensors that are invariant under space inversion $\bar{1}$ but also holds for those that change sign under $\bar{1}$. The result can be generalized to limiting point groups (LPGs, which contain ∞-fold rotation axes) and to magnetic point groups.

Tensors describing material properties are invariant under the point group of the material under consideration. This requirement puts restrictions on the form of the tensor that depend on its rank, internal symmetry, and its behaviour under $\bar{1}$. Ordinary tensors of even rank and pseudo tensors of odd rank are invariant under $\bar{1}$ (i-tensors); ordinary tensors of odd rank and pseudo tensors of even rank change sign under $\bar{1}$ (c-tensors). The form of an i-tensor depends only on the Laue class of the material under consideration, which is determined by the group generated by $\bar{1}$ and the point group of the material. A c-tensor vanishes for all point groups that contain an element $\bar{1}$. There are ten CPGs and one LPG that contain $\bar{1}$ only in combination with rotations different from the identity. For these groups, the form of c-tensors is given by the following formulae:

$$
\begin{array}{llll}
T_m = T_1 - T_2 & T_{\bar{4}} = T_2 - T_4 & & \\
T_{mm2} = T_2 - T_{222} & T_{\bar{6}} = T_3 - T_6 & & \\
T_{3m} = T_3 - T_{32} & & & \\
T_{4mm} = T_4 - T_{422} & T_{\bar{4}2m} = T_{222} - T_{422} & (T_{\bar{4}m2} = T_{mm2} - T_{4mm}) & (1) \\
T_{6mm} = T_6 - T_{622} & (T_{\bar{6}2m} = T_{32} - T_{622}) & T_{\bar{6}m2} = T_{3m} - T_{6mm} & \\
T_{\bar{4}3m} = T_{23} - T_{432} & & & \\
T_{\infty m} = T_{\infty} - T_{\infty 2} & & &
\end{array}
$$

where T_G denotes the form of a c-tensor of given rank and internal symmetry that is invariant under the point group G. The first tensor on the right hand side can be uniquely written as a sum of the tensor on the left hand side and of the second tensor on the right. To give an example: any tensor of form T_3 can be uniquely written as a tensor of form T_{3m} and one of form T_{32}. This implies that tensors T_{3m} and T_{32} have only the vanishing tensor in common. The Hermann-Mauguin symbols for the point groups fix the orientation of the symmetry elements as stated in Table 12.2 of [1] with **c** unique for the monoclinic point groups. ($T_m = T_1 - T_2$ is valid also for **b** unique.) A proof of the above relations for the CPGs can be found in [2]. It follows from a theorem due to C. Hermann (see e.g. [3]) that $T_\infty = T_6$, $T_{\infty 2} = T_{622}$, and $T_{\infty m} = T_{6mm}$ for tensors of rank $r < 6$.

The formulae (1) can be used for example to determine all forms of a c-tensor if the forms of the i-tensor of the same rank and internal symmetry are known, because both tensors have the same form for pure rotation groups. Let us illustrate this with a simple example: The symmetric tensor of second rank that describes for example dielectric and magnetic susceptibility, electric and thermic conductivity has for 2 || z and for 4 the forms:

$$T_2 = \begin{pmatrix} T_{11} & T_{12} & 0 \\ & T_{22} & 0 \\ & & T_{33} \end{pmatrix}, \quad \text{and} \quad T_4 = \begin{pmatrix} T_{11} & 0 & 0 \\ & T_{11} & 0 \\ & & T_{33} \end{pmatrix}.$$

Formula (1) for $T_{\bar{4}}$ tells us then that the gyration tensor G, which describes optical activity, and is a symmetric pseudo tensor of second rank has the form:

$$G_{\bar{4}} = \begin{pmatrix} G_{11} & G_{12} & 0 \\ & -G_{11} & 0 \\ & & 0 \end{pmatrix}.$$

Use has been made of the fact that a tensor with arbitrary values of T_{11} and T_{22} may be uniquely written as the sum of two tensors with $T'_{22} = T'_{11}$ and $T''_{22} = -T''_{11}$, respectively. The relations (1) provide a quick test for existing tables of the forms of property tensors that change sign under $\bar{1}$ and will be helpful for the computation of new tables for higher order effects that become accessible to measurement with improved experimental techniques. Examples are given in [2], where also the generalization of the relations (1) to magnetic point groups can be found.

This generalization will be given here for the limiting point groups [3]. A tensor is either invariant under space inversion $\bar{1}$, time inversion $1'$ and space-time inversion $\bar{1}'$ (i-tensor) or it is invariant for one of them and changes sign for the other two: an s-tensor is invariant under space inversion, a t-tensor under time inversion and a u-tensor under space-time inversion. The form of an i-tensor depends only on the Laue class, i.e. an i-tensor has the same form $T_{\infty\infty}$ for the 5 isotropic LPGs $\infty\infty m1'$, $\infty\infty m$, $\infty\infty 1'$, $\infty\infty m'$ and $\infty\infty$, it has the same form T_∞ for the 5 LPGs $\infty/m1'$, ∞/m, $\infty 1'$, ∞/m' and ∞, and it has the same form $T_{\infty 2}$ for the remaining 11 LPGs $\infty/mm1'$, ∞/mm, $\infty 21'$, $\infty/m'm'$, ∞/mm', $\infty m1'$, $\infty/m'm$, $\infty 2$, ∞m, $\infty 2'$, and $\infty m'$. The forms of the non-vanishing tensors of types s,t and u are given in the following table.

Form	Type		
	s	t	u
T_∞	∞, ∞/m	∞, $\infty 1'$	∞, ∞/m'
$T_{\infty 2}$	$\infty 2$, ∞m, ∞/mm	$\infty 2$, $\infty 2'$, $\infty 21'$	$\infty 2$, $\infty m'$, $\infty/m'm'$
$T_\infty - T_{\infty 2}$	$\infty 2'$, $\infty m'$, ∞/mm'	∞m, $\infty m'$, $\infty m1'$	∞m, $\infty 2'$, $\infty/m'm$
$T_{\infty\infty}$	$\infty\infty$, $\infty\infty m$	$\infty\infty$, $\infty\infty 1'$	$\infty\infty$, $\infty\infty m'$

References

[1] *International Tables for Crystallography.* (1983). Vol. A. Dordrecht: Reidel.

[2] H. GRIMMER, *Acta Cryst.* A (accepted for publication).

[3] Y. SIROTINE, M. CHASKOLSKAÏA, *Fondements de la Physique des Cristaux* (Mir, Moscow, 1984).

INTERFACE-CONFINED ORDERED COMPOUND FORMATION: APPLICATION TO Si/Ge STRAINED HETEROJUNCTIONS

K. A. Mäder[1,2], H. von Känel[1], and A. Baldereschi[2,3]
[1]Laboratorium für Festkörperphysik, ETH, CH-8093 Zürich
[2]Institut de Physique Appliquée, EPF, CH-1015 Lausanne
[3]IRRMA, PH - Ecublens, CH-1015 Lausanne

We introduce a model for the study of the atomic structure of semiconductor interfaces which takes into account both strain and chemical energies. The two effects are generally in competition with each other for lattice mismatched heterostructures. According to the model, space-confined ordered intermixing, limited by enthalpy rather than diffusion, can occur at the interface in spite of bulk instability of the new phase.

Unintentional atomic order has been observed in the past in various MBE grown III-V semiconductor alloys. The existence of these epitaxial ordered phases is currently explained in terms of the elastic energy associated with internal strains. Recently, unintentional ordering confined to a few atomic layers only, has also been observed at Si | Ge interfaces [1]. Here we propose an explanation of the latter experimental observations in terms of competing elastic and chemical energies and the fact that the relative role of these energies near interdiffused junctions is different from that in the bulk.

Our model for the enthalpy H of an ordered compound $\gamma\text{-}A_pB_q$, where A and B are diamond-like semiconductors, contains the following ingredients: an elastic energy $E_s(\gamma\text{-}A_pB_q)$ which is treated in the valence force field (VFF) approximation, and a chemical energy $E_{\text{chem}}(\gamma\text{-}A_pB_q)$, which is the sum over all AA, BB, and AB pairs of the corresponding bond chemical energies. The most relevant parameter of the model is $\Delta\varepsilon$, the excess chemical energy of the AB heterobond with respect to the arithmetic mean of the AA and BB homobonds.

For a given bulk ordered phase $\gamma\text{-}A_pB_q$ and for a given strain condition imposed by the substrate, the model predicts bulk ordering for $\Delta\varepsilon < \Delta\varepsilon_c{}^{\infty}(\gamma)$, where $\Delta\varepsilon_c{}^{\infty}(\gamma)$ is a critical value of the chemical energy, which depends on the internal strains and is a function of the VFF parameters.

This bulk condition does not apply at the junction due to interface specific phenomena. For the interface-confined ordering we compare the enthalpy of a sharp A | B interface with that of an interdiffused $A\,|\,(\gamma\text{-}A_pB_q)_m\,|\,B$ one, where m is the number of the ordered atomic intralayers. In this case the critical chemical energy is $\Delta\varepsilon_c{}^{m}(\gamma)$, which converges to $\Delta\varepsilon_c{}^{\infty}(\gamma)$ for increasing m, but deviates from it for small m since the number of heterobonds which are formed at the interdiffused

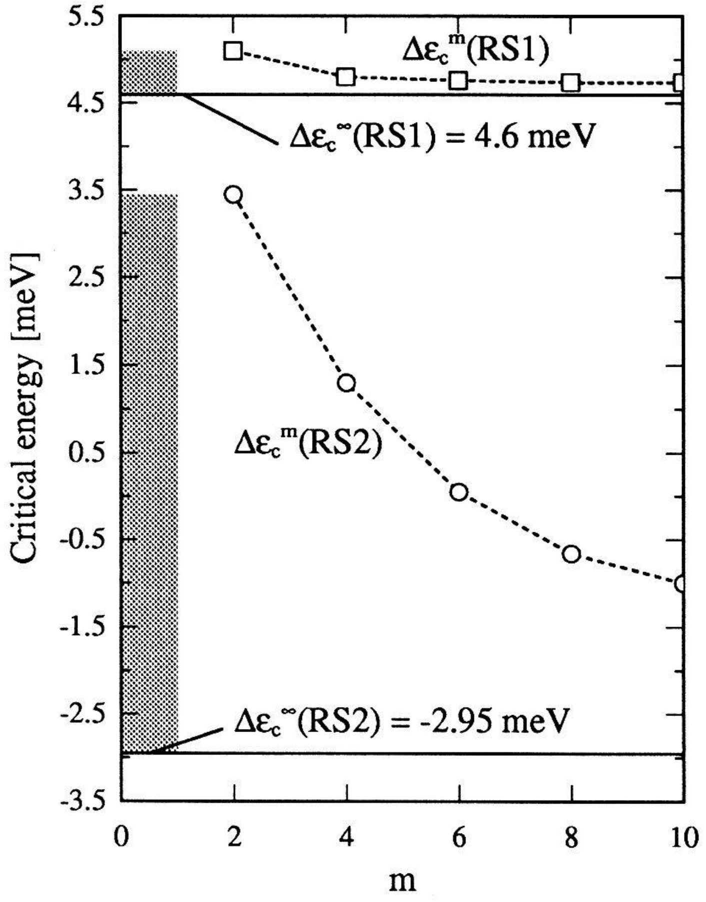

junction depends on m. Thus, if $\Delta\varepsilon_c^\infty(\gamma) < \Delta\varepsilon < \Delta\varepsilon_c^m\gamma)$, the ordered intralayer is expected to form in spite of the instability of the bulk phase γ-A_pB_q. For the rhombohedral structures RS1 and RS2 of SiGe discussed in detail elsewhere [2], known values of $\Delta\varepsilon$ [3] are indeed close to the critical energies obtained by our model. In the figure the critical chemical energies $\Delta\varepsilon_c^m(\gamma)$ are displayed for rhombohedrally ordered SiGe intralayers on a Ge (001) substrate, and capped with epitaxial Si (001). The asymptotic values $\Delta\varepsilon_c^\infty(\gamma)$ = 4.6 meV and -2.95 meV per bond for γ = RS1 and RS2, respectively, which result from our VFF parameters are also indicated (solid lines). The energy ranges where interface-confined ordering is predicted are shaded. Note the rather narrow interval in the case of RS1 as compared to RS2. The RS2 phase is highly strained in its equilibrium form, whereas a few layers can accommodate strain more easily, hence the rather slow convergence of $\Delta\varepsilon_c^m$(RS2). The RS1 phase on the other hand is unstrained in its bulk form, and the strain release is more continuous as a function of m.

In experiment [4] RS1 is found to be a reversible (strained) phase with a transition temperature of about 700 °C. The RS2 type of order is only found in as-grown alloy films and superlattices and is probably due to growth-specific effects at the (001) surface [5]. Interface-confined ordering as predicted by our model could then lead to an enhanced stability of the as-grown structure.

[1] E. Müller, H.-U. Nissen, M. Ospelt and H. von Känel, Phys. Rev. Lett. **63**, 1819 (1989)
[2] K. A. Mäder, H. von Känel, and A. Baldereschi, Superlattices and Microstructures, in press
[3] J.L. Martins and A. Zunger, Phys. Rev. Lett. **56**, 1400 (1986)
[4] E. Müller, H.-U. Nissen, K. A. Mäder, M. Ospelt, and H. von Känel, to be published.
[5] F. K. LeGoues, V. P. Kesan, S. S. Iyer, J. Tersoff, and R. Tromp, Phys. Rev. Lett. **64**, 2038 (1990)

FORMATION OF ELECTRICAL BREAKDOWN IN A SILENT DISCHARGE. ONE - DIMENSIONAL CALCULATIONS.

W. Egli and B. Eliasson
ASEA Brown Boveri, Corporate Research, CH-5405 Baden, Switzerland

Introduction

We present simplified calculations of electrical breakdown in a plane-parallel gap, where one of the electrodes is covered by a dielectric. The only spatial dimension considered is the direction perpendicular to the electrodes. The two-dimensional version has been published elsewhere ([1], [2], for the geometrical setup see Fig. 1 in [1]). Although with such a model, one cannot calculate such important parameters as total charge transported by the breakdown channel, the model contains most of the important characteristics of the breakdown itself. Because of its simplicity such a model is a fast and relatively easy way to evaluate breakdown numerically. With the model one can also simulate the temporal behaviour of a number of microdischarges occurring either simultaneously at different intervals in time.

The Model

We solve the equation of continuity for each species (electron, positive and negative ions) with the appropriate boundary conditions [2]. Additionally, we solve the Poisson equation to obtain the electric field. The method of solution was described in detail in Ref. [1].

Some solutions

In the following examples the metal electrode is the cathode ($z = 0$) and the dielectric is the anode ($z = d$). In course of the breakdown a charge is deposited on the dielectric. This charge build-up and the field it induces leads to the extinguishing of the breakdown and a formation of a current pulse.

In Fig. 1 we have shown both the electric field as well as the electron density as a function of time. In case of the electron density the propagation of an avalanche towards the dielectric is very well visible. One can in both instances (field and electron density) see the formation of a reflected wave and its propagation towards the cathode.

The shape of the current pulse due to the transport of charge towards the dielectric depends to a large degree on the dielectric constant of the dielectric layer and the applied field. The higher the dielectric constant the greater the probability that a second peak appears. The first peak is due to the primary avalanche. A second peak can appear if the reflected wave creates enough additional electrons in the gap. Once these are brought to the dielectric surface a second peak appears. The same effect one obtains by applying larger field to the gap. This effect is shown in Fig. 2.

The charge density depends on the gas used, the applied field, the geometry of the gap and the dielectric constant. In Fig. 3 we show for 3 different gases the dependence of the charge density on the applied field relative to the respective Paschen field (E_0). The charge increases with increasing field and furthermore depends inversely on the derivate of the effective ionization curve with respect to the reduced field E/n. Both of these results are in agreement with the results presented in Ref. [3].

References

[1] W. Egli, B. Eliasson, Numerical Calculation of electrical Breakdown in Oxygen in a Dielectric - Barrier Discharge. Helvetica Physica Acta, Vol. 62 (1989).

[2] B. Eliasson, W. Egli, The Silent Discharge, Numerical Simulation of microdischarge formation. Int. Conference on Phenomena in Ionized Gases (ICPIG XIX) Belgrade, 10-14 July 1989.

[3] B. Eliasson, S. Strässler, Calculation of the Charge and Radius of Breakdown Channels in Gases at Atmospheric Pressure. Bull.Am.Phys.Soc. 18, 183 (1983).

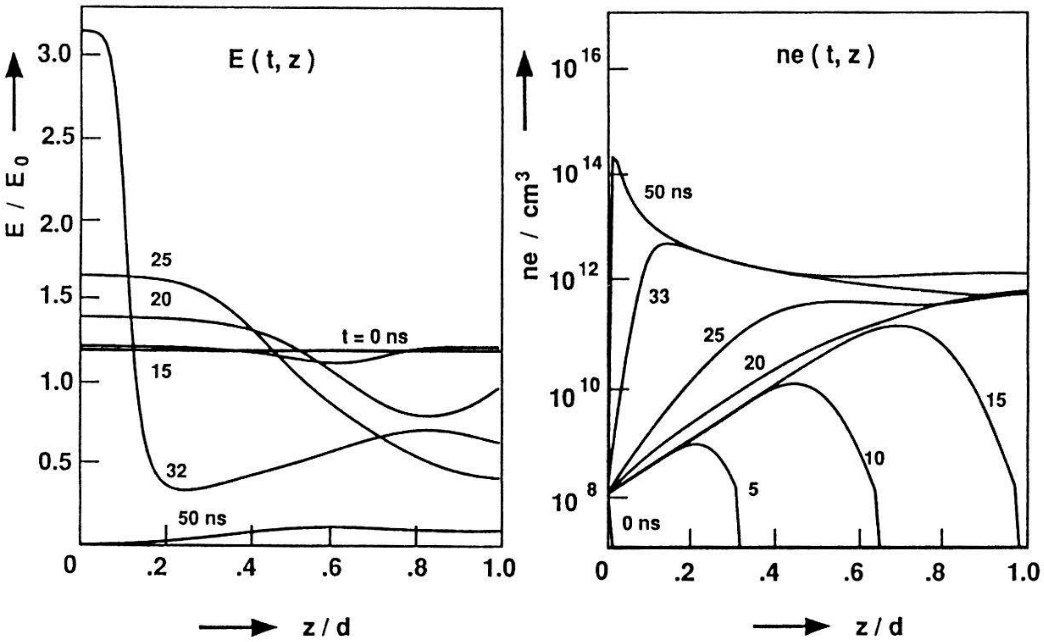

Fig. 1 The development of the electric field and the electron density as a function of the axial coordinate and time in Xenon. The applied field was E/n = 20 kV/cm, the gap width d = 1 mm, thickness of the dielectric g = 0.8 mm, $\varepsilon_r = 3$ and the pressure 1 bar.

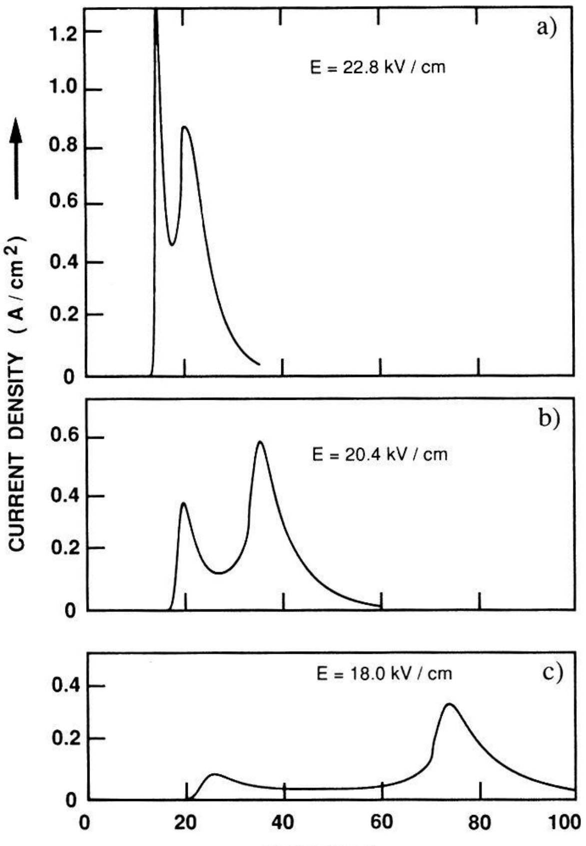

Fig. 2 Current density vs. time for 3 different values of the applied field. The parameters are the same as in Fig. 1.

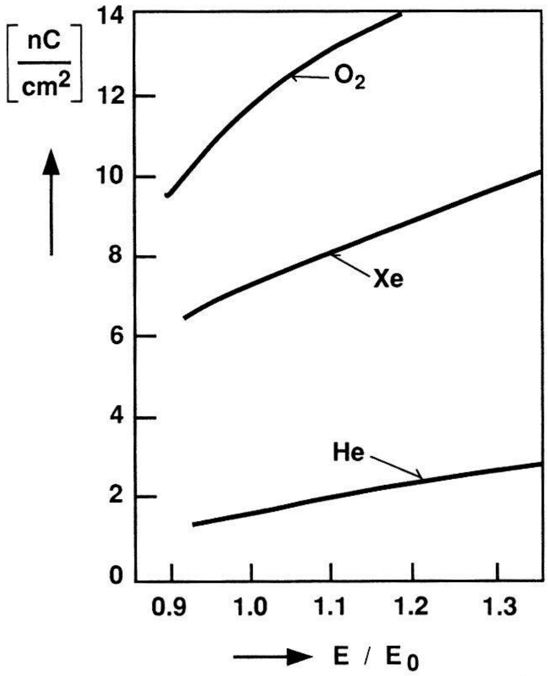

Fig. 3 Charge density for 3 different gases versus electric field.

A CCD Based Electron Counting System for High Energy Electrons

B. D. Hall and R. Monot

Institut de Physique Expérimentale, EPFL, 1015 Lausanne, Switzerland.

A CCD based electron counting system has been developed for high energy electrons (20 - 100 kV). The system operates in a direct electron bombardment mode, using the gain in secondary charge to identify single events. The system electronics and performance are presented.

There is considerable interest, in the field of cluster and ultrafine particle research, in experimental techniques that enable physical structure determination for nanometre sized particles, or smaller. Electron diffraction on a molecular beam containing ultrafine particles is one such technique, and an experimental apparatus of this type has been developed in Lausanne [1]. Recently, in order to improve the performance of this apparatus, the electron illumination system and detection electronics have been replaced. We describe here the new detection system, information concerning the other changes to the apparatus are awaiting publication [2].

The new detection system is based on a pair of linear CCD imagers (Texas Instruments VID-283) operated in a direct electron bombardment mode. The diffraction patterns to be recorded are of the Debye-Scherrer type, with concentric rings of intensity being formed on the image plane. The detectors are placed, symmetrically, on either side of the central beam, so as to record the intensity profile of these rings along a diametrical section.

High energy electrons impinge directly on the surface of the detector, penetrate a thin oxide layer and continue into the device, generating a large secondary charge as they loose energy. Charge build up in the on-chip device electronics will quickly lead to device failure, however, the sensitive regions of the device can be effectively protected using mechanical slits, leaving only the photosites exposed to the electron flux.

Single event counting is made possible by the large effective gain due to the generation of secondary charge ($\sim 10^4 - 10^5$). A discriminating accumulator has been designed to operate the detection system in this way. Because of inhomogeneous dark signals in the CCDs' photosites, the lower window for discrimination must be assigned to each pixel individually. These values are estimated by measuring the average dark current in each pixel which is then stored in the accumulator reference memory. During signal accumulation the CCD output is sequentially compared with these reference values and, when the measured signal is superior to the reference plus a common offset, a pixel event counter is incremented accordingly.

Successful single event counting also relies on correct exposure of the detectors to the electron flux between CCD readings. CCD photosites must be read out sequentially, meaning than the whole device must be read out to obtain information on individual photosites. Too much intensity between readings will lead to pile-up. Too little intensity will waste accumulation time in reading out empty pixels. To achieve exposure control the incident electron beam is blanked by an electrostatic shutter. The duty cycle of this shutter can be varied under computer control, allowing easy optimization of the exposure time.

Special attention has been given to noise sources in the CCD imagers. Tri-level clocking has been employed on the clock signal controlling the gating and reset of the charge sensitive output node. This allows double correlated sampling to be implemented which eliminates reset noise [3, 4]. A second source of noise (the spurious 'hot hole' noise effect [5]), particular to the Virtual Phase technology CCDs, has been successfully reduced using bi-level, long risetime clock signals on the CCD transport registers instead of tri-level clocking.

Radiation damage, due to a build up of charge in the oxide layer above the CCD registers, has been observed but is found to be acceptably small. The type of CCD technology chosen (Texas Instruments Virtual Phase) is known to be relatively radiation hard and can support in excess of 1 Mrad [6]. In our application, such exposure corresponds to roughly 100 hours of sustained operation.

References

[1] B. Hall, M. Flüeli, R. Monot and J. -P. Borel, Helvetica Physica Acta **61**, 193 (1988).

[2] B. D. Hall, D. Reinhard, J. -P. Borel and R. Monot, Zeit. Phys. D. *in press.*

[3] F. E. Stuart and D. L. Bass, Kitt Peak National Observatory R&D Technical Memorandum, No. 1, May 4, (1983).

[4] J. Hynecek, IEEE Trans. Electron Devices, **33**, 850 (1986).

[5] J. Hynecek, IEEE Trans. Electron Devices, **30**, 940 (1983).

[6] R. D. McGrath, IEEE Trans. Nuclear Sci., **28**, 4028 (1981).

DETERMINATION OF ELASTIC PROPERTIES OF SI/GE SUPERLATTICES FROM SURFACE ACOUSTIC MODES BY BRILLOUIN SCATTERING

M. MENDIK, M. OSPELT, H. VON KÄNEL, P. WACHTER
Lab. für Festkörperphysik, ETH–Zürich, 8093 Zürich

Abstract

Surface acoustic waves (SAW) on epitaxially grown strained–layer Si/Ge superlattices (SLs) on Si(100) have been studied by means of Brillouin scattering. The SLs have been treated as media with effective elastic constants since the wavelength λ of the thermally excited Rayleigh wave is longer than the SL–period Λ. The investigated SLs have had nearly similar SL–periods but different Ge–contents.

Introduction

The existence of a surface causes interference of shear and compressional bulk waves at the crystal–air interface and is therefore the origin of SAWs. These corrugations, propagating at the surface, are the dominating mechanism for light scattering in opaque media. It was first demonstrated by Elmiger [1] that it is possible to compute the complete elastic tensor of cubic single crystals using the angular dependence of SAWs (without knowing the optical constants).

Experimental

We used the TM polarized λ=514 nm line of an Ar^+ laser as the excitation source with an incident power of 80 mW. The backscattered light was analysed by a (3+3) tandem interferometer, described in [2]. For the experiments the samples were in air and at room temperature and no effect of heating was observed. By varying the incident angle ϑ_i form 45° to 70° it is possible to control the length of k of the selected SAW, while rotating the sample around the normal (ϑ_i constant) allows to select the direction of the phonon momentum in the sample plane. Several Si/Ge SLs of various thicknesses and compositions were epitaxially grown on Si(100) substrates and characterized by Rutherford backscattering and channeling and X–ray diffraction [3]. We studied SLs with thicknesses h_1=6795(SL5071), h_2=5693(SL5072), h_3=5084Å (SL5073) and similar SL periods Λ_1=14, Λ_2=12, Λ_2=11 Å but with different thicknesses of the Ge–contents d_{Ge1}=4.7, d_{Ge2}=3.1 and d_{Ge3}=1.7 Å.

Measurements

A film grown on a substrate loads of stiffens the surface. If the layer is thinner than the penetration depth of a SAW (5000 Å in the GHz range) the velocity depends on the elastic properties of the substrate as well as on those of the film. In contrast, if the film is sufficiently thick the SAW is completely decoupled from the substrate. No measurable influence of the substrate has been found in our samples. Fig) shows the angular dispersion of the SAW on all samples. The axes indicated on the plot refer to the crystallographic direction of the substrate. The angular dependence of the velocity reflects the cystallographic symmetry of the film (which happens to be cubic as well in our case). Moreover the increasing Ge concentration causes softening of the surface acoustic phonon.

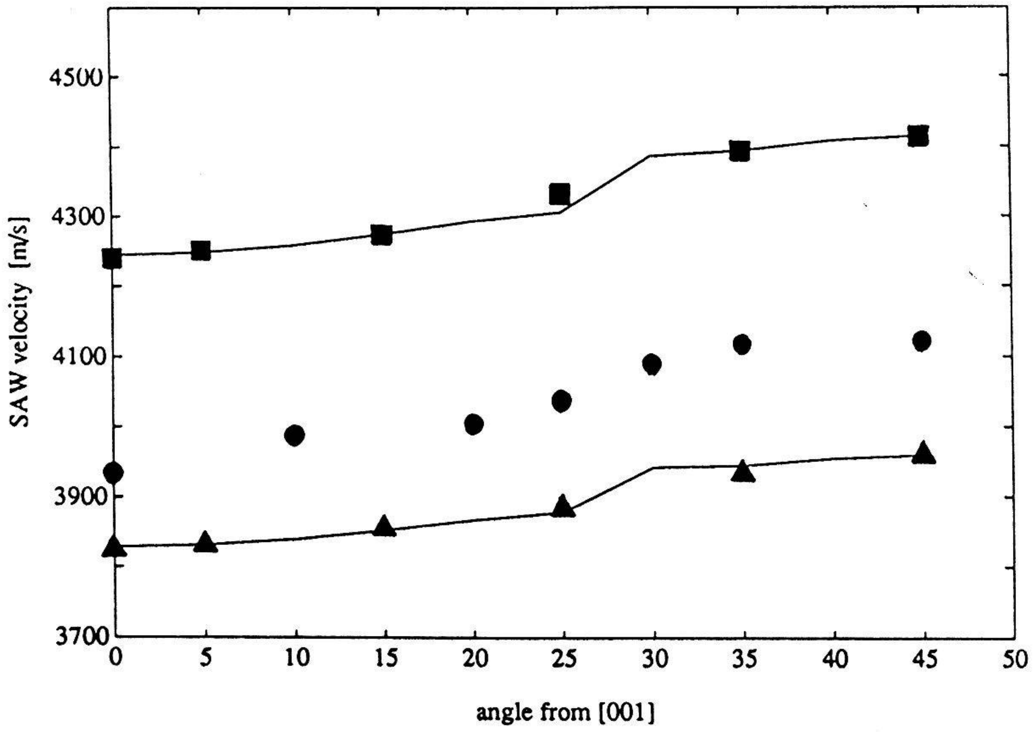

Fig) Angular dispersion of the SAW on SL5071 ▲ ,SL5072 ● ,SL5073 ■ (all (100))

Computations

The investigated SLs can be treated as media with effective elastic constants derived from their constitutents Si and Ge since the wavelength of the thermally stimulated SAW (> 3000 Å) is longer than the SL period [4]. The whole SL has been assumed to have cubic symmetry neglecting the slight tetragonal distortion. The density of each SL has been linearly interpolated between the one of its constitutents. (ρ_{Si} = 2.33 gr/cm^3; ρ_{Ge}=5.32 gr/cm^3). In order to get the effective elastic tensor we applied the Levenberg–Marquardt procedure to perform a least squares fit of the model function described in [5]. The elastic constants thus derived are:

SL5071 : C11=142.9±2.8GPa (145), C44=68.1±2.0GPa (69), C12=56.4±2.7GPa (53)
SL5073 : C11=147.0±3.0GPa (150), C44=73.0±2.2GPa (72), C12=59.0±2.8GPa (56)

In brackets are shown for comparison the similar values obtained by linear interpolation of the elastic constants of single crystal Si and Ge [1] determined by the same procedure.

References

[1] M.W. Elmiger, Surface and Interface Analysis, 14, 18 (1989)
[2] J.R. Sandercock in "Light Scattering in Solids II", p. 173, Springer (1982)
[3] M .Ospelt, Superlattices and Microstructures, 5, 71, (1989)
[4] M. Grimsditch, Phys. Rev. B 31, 6818 (1985)
[5] G.W. Farnell in "Physical Acoustics" VI, p. 109; Ed. Mason, Academic Press (1970)

Structural and Electrical Investigation of an Epitaxial Metallic $FeSi_2$ - Phase on Si (111)

N. ONDA[1], J. HENZ[1], E. MÜLLER[1], H. VON KÄNEL[1]
C. SCHWARZ[1], R. E. PIXLEY[2]
[1]Laboratorium für Festkörperphysik, ETH, 8093 Zürich,
[2]Physik - Institut der Universität Zürich, 8001 Zürich

An epitaxial $FeSi_2$ phase of cubic symmetry has been grown on Si (111) by molecular beam epitaxy (MBE). Reflection high energy electron diffraction (RHEED) and high-resolution transmission electron microscopy (TEM) suggest the phase to have CaF_2 structure. Ultraviolet photoelectron spectroscopy (UPS) and resistivity measurements show that the phase is metallic and undergoes an irreversible metal / semiconductor transition to the ß-$FeSi_2$ phase at a temperature depending on the thickness of the films.

For years great attention has been paid to the epitaxial growth of silicon-rich metal silicides with fluorite structure, i.e. $NiSi_2$ and $CoSi_2$, because of their fundamental and technological importance. Especially on Si (111) epitaxial films with excellent properties have been realized [1]. While employing the same techniques for the epitaxial growth of $FeSi_2$ on Silicon (111), we found a new, hitherto unknown phase of this silicide.

In the following the new $FeSi_2$-phase which is stabilized by the epitaxial constraint, will be shown to exhibit properties surprisingly close to those of $NiSi_2$ and $CoSi_2$.

As substrates we used (111)-oriented, n-doped (1 Ωcm-2000 Ωcm) 3 inch diameter Si-wafers. They were first precleaned by the "Shiraki" method and heated *in situ* to 830°C under a weak silicon flux to desorb the oxide. The $FeSi_2$ - layers were grown in two steps. The first one consisted in coevaporating a 10Å thick Fe- and Si-layer stoichiometrically (1:2), followed by annealing to 400-450°C.

At 250°C an epitaxial cubic phase of $FeSi_2$ begins to form as can be inferred from the Kikuchi pattern observed by RHEED. The thickness of the silicide can be increased in a second step by MBE at room temperature. Upon annealing an irreversible phase transition to the orthorhombic ß-$FeSi_2$ is seen to occur. The temperature at which the transition takes place depends on the thickness of the layers. The thinnest ones (14Å) are stable to temperatures up to 500°C while the thicker ones (300Å) are transformed above 200°C.

It has been noted before [2] that the orthorhombic ß-$FeSi_2$ phase can be derived from the CaF_2 structure by a small distortion.

This leads us to the assumption that the observed phase does have fluorite structure indeed. The observed Kikuchi-map is in agreement with such an assignment. Moreover, the silicide is seen to be rotated around the [111] surface normal, giving rise to the same type B orientation as has been observed, e.g. in the case of $CoSi_2$. Rutherford backscattering revealed that the <114> channeling minimum of the Si substrate is displaced by 0.42° from the <110> channeling minimum of a 70 Å thick film, indicating a slight distortion from the cubic symmetry.

Cross-section TEM showed that the interfaces are of a similar quality as has been demonstrated previously for $NiSi_2$ and $CoSi_2$ [1].

The described phase transition from the cubic low temperature phase to the ß-$FeSi_2$ -phase is accompanied by a marked change of the electrical properties. In fig.1 are displayed the UPS spectra before (a) and after (b) this phase transition. The low temperature phase is metallic in accordance with theoretical calculations [3] based on the assumed CaF_2 -structure. By contrast ß-$FeSi_2$ is a semiconductor.

The electrical resistivity (≈450 μΩcm) of the metallic phase is nearly temperature independent indicating that the mobility is governed by defect scattering.

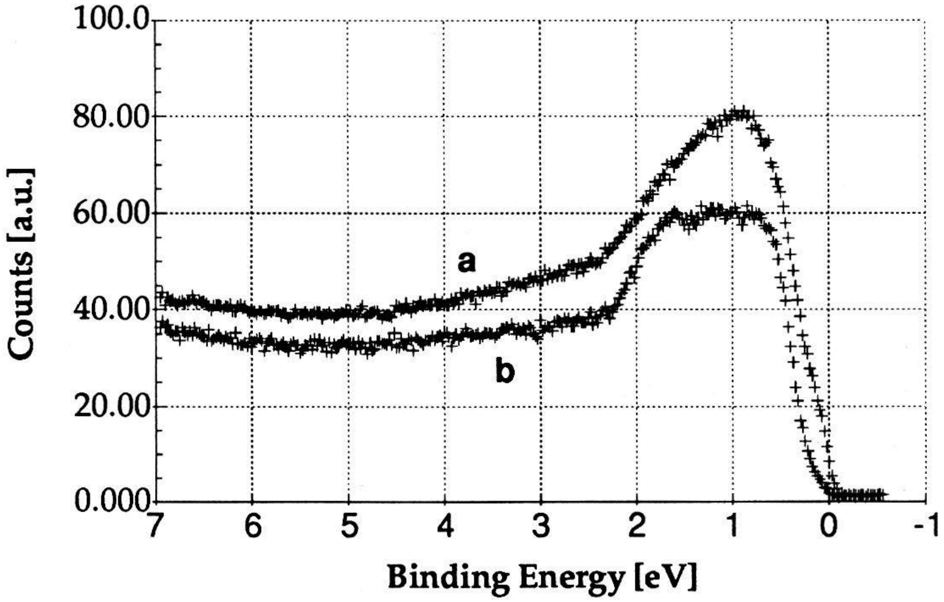

Fig.1: *UPS spectra taken with He I radiation of cubic* $FeSi_2$ *(a) and ß-*$FeSi_2$ *(b).*

[1] H. von Känel, J. Henz, M. Ospelt, J. Hugi, E. Müller and N. Onda, *Thin Solid Films, 184 (1990)*

[2] H.C. Cheng, L.J. Chen, and T.R. Your, *Mat. Res. Soc. Symp. Proc. Vol. 25 (1984) and references therein.*

[3] K. Mäder, *private communication*

A New Approach of the Bound State Problem in Quantum Field Theory

Etienne Frochaux
Département de Mathématiques, EPFL, 1015 Lausanne

We are interested in the quantum and relativistic two-particle system at low energy, especially the bound states, within the framework of the Quantum Field Theory. To begin this study, we work with the simplest Q.F.T. models with effective interaction, the weakly-coupled $\mathcal{P}(\varphi)_2$ models. They are formally given by the Lagrangian density

$$\mathcal{L} = \frac{1}{2}\left((\partial_0\varphi(x))^2 - (\partial_1\varphi(x))^2 - m_0^2\varphi(x))^2\right) - \lambda\mathcal{P}(\varphi(x))$$

where $\varphi : R^2 = R_{time} \times R_{space} \rightarrow R$ is the field, $m_0^2 > 0$ the bare mass of one particle, $\lambda \geq 0$ the coupling constant and $\mathcal{P}$ the interaction polynomial (positive valued). The "weak coupling" means that $\lambda/m_0^2 \ll 1$. The mathematical construction of these models has been obtained by Glimm, Jaffe and Spencer [1], and it has been proved that they describe a world in which interaction indeed occurs [1]. The spectrum of the mass operator M, given by $M^2 = H^2 - P^2$ where H is the hamiltonian and P is the total momentum, has been obtained by Eckmann and al. [2] from the analysis of the so-called Bethe-Salpeter equation, and is the following :

First we find two isolated eigenvalues, 0 (the corresponding eigenspace is one-dimensional and is generated by the vacuum state Ω) and $m > 0$, the one-particle mass (which depends on λ). For some polynomial $\mathcal{P}$ we can find a third eigenvalue m_B close to $2m$ and smaller than $2m$. Moreover $m(\lambda)$, $m_B(\lambda)$ are C^∞ functions of λ satisfying $m \rightarrow m_0$ and $m_B \rightarrow 2m_0$ when $\lambda \rightarrow 0$. m_B is interpreted as the mass of a two-particle bound state.

An other method for finding the bound states, called the *variational perturbation method*, initially proposed by Glimm, Jaffe and Spencer, is presented here. The bound-state mass m_B is defined by the infimum of a Rayleigh quotient :

$$m_B^2 = \inf_{\psi \neq 0, \psi \in \mathcal{V}} \frac{\langle\psi; M^2\psi\rangle}{\langle\psi;\psi\rangle}$$

where $\mathcal{V}$ is the intersection of the domain of M and the subspace orthogonal to the vacuum and the one-particle states. But $\mathcal{V}$ can also be replaced by any subspace $\mathcal{W}$ dense in $\mathcal{V}$. Recall that m_B is a C^∞ function of λ. If we restrict ourselves to a perturbation calculation, $\mathcal{W}$ can be replaced by any subspace $\mathcal{U}$ of $\mathcal{W}$ for which $\langle\psi; M^2\psi\rangle/\langle\psi;\psi\rangle$ gives up to higher order terms the same values. We have found (see [3],[4]) that the span of the vectors

$$\Psi(\{f_m^0\},\{f_m^1\},\ldots,\{f_m^K\}) = \sum_{n=0}^{K} \lambda^n \sum_{m \in N} :\Theta^m(f_m^n):\Omega$$

where Θ^m describe zero-time fields of degree m and : . : means the Wick ordering, satisfies this property at order $O(\lambda^{K+1})$, for functions f_m^n in some function spaces $\mathcal{F}_m$. Some of the above functions f_m^n are determined by the orthogonality with respect to the vacuum and one-particle states, more precisely to have $\| (1 - E_0 - E_m)\Psi - \Psi \| = O(\lambda^{K+1})$, where E_μ is the projector associated with the eigenvalue μ of M. We put such a vector $\Psi(\{f_m^0\},\{f_m^1\},\ldots)$ in the Rayleigh quotient and begin the minimalization. First we look at the case where $\lambda = 0$ which immediately imposes $f_m^0 = 0$ for all $m \neq 2$. Putting $f = f_2^0$, we obtain the equation

$$m_B^2 = \inf_{f,\{f_m^1\},\{f_m^2\},\ldots} \frac{\langle f; M^2 f\rangle + \lambda 2\Re \sum_m \langle f; M^2 f_m^1\rangle + \lambda^2 \sum_{m,n}\langle f_m^1; M^2 f_n^1\rangle + \ldots}{\langle f; f\rangle + \lambda 2\Re \sum_m \langle f; f_m^1\rangle + \lambda^2 \sum_{m,n}\langle f_m^1; f_n^1\rangle + \ldots} + O(\lambda^{K+1})$$

where we have adopted the notation $\langle : \Theta^m(g) : \Omega; M^2 : \Theta^m(h) : \Omega\rangle = \langle g; M^2 h\rangle$, etc ... Now we first begin to minimize the r.h.s. by varying the functions f_m^1, f_m^2,... but not the function f. This programme leads to well defined functions $f_m^1(f)$, $f_m^2(f), \ldots$ (which depend on f), and we are left with the equation, at first perturbation orders :

$$m_B^2 = \inf_{0 \neq f \in \mathcal{F}_2} \frac{1}{2\int d\sigma(p) \mid f(p) \mid^2} \Big[2 \int d\sigma(p) \mid f(p) \mid^2 \mathcal{M}(p)^2 +$$

$$+ \frac{1}{2} \int d\sigma(p) d\sigma(p') \overline{f(p)} f(p') \mathcal{B}(p,p')(\Omega(p) + \Omega(p'))\delta(p_1 + p_2 - p_1' - p_2')\Big] + O(\lambda^{\nu+1})$$

where $d\sigma(p) = dp_1\, dp_2 / 2\omega(p_1) 2\omega(p_2)$, $\omega(p_i) = \sqrt{p_i^2 + m^2}$ for $i \in \{1,2\}$ (recall that m depends on λ), $\Omega(p) = \omega(p_1) + \omega(p_2)$, $\mathcal{M}(p)^2 = \Omega(p)^2 - (p_1 + p_2)^2$, and $\mathcal{B}(p,p')$ is the Bethe-Salpeter kernel (or the kernel which plays the same role when $\mathcal{P}$ is not even) on the mass shell, at first non-vanishing perturbation orders ($\nu = 1$ or 2, depending on $\mathcal{P}$). The above equation has been obtained with the help of the following *condition for low relative energy*

$$\frac{\int d\sigma(p) \mid f(p) \mid^2 \mathcal{M}(p)^2}{\int d\sigma(p) \mid f(p) \mid^2} - (2m)^2 < \lambda^\nu K$$

for some constant K. The equality in the above equations for m_B^2 must be explained (we would expect $\leq$ instead of $=$). It holds because the infimum in the r.h.s. gives exactly the same result as the Bethe-Salpeter method at first perturbation orders (see [3], [5]).

It is instructing to make a change of representation of the state space, by introducing for every function f a new function F such that $\| \Psi(f, \{f_m^1(f)\}, \ldots) \|^2 = \int d\sigma(p) \mid F(p) \mid^2$, and then to write the scalar products $\langle \Psi; P\Psi\rangle$, $\langle \Psi; H\Psi\rangle$ and $\langle \Psi; L\Psi\rangle$ (L is the Lorentz generator) as bilinear functions of F. The operators which generate these forms can be given as follows.

The Hilbert state space is now the asymptotic subspace $\mathcal{H} = L^2(R^2, \sigma)$.

The total momentum is a multiplication operator : $PF(p) = (p_1 + p_2)F(p)$.

H and L are given by $H = \Omega + \{\Omega, \mathcal{O}\}$ and $L = L_0 + \{L_0, \mathcal{O}\}$, with the notation $\{A, B\} = AB + BA$, where Ω is the multiplication operator by $\Omega(p)$, L_0 is the Lorentz generator of the asymptotic theory and the *interaction operator* $\mathcal{O}$ is given by

$$\mathcal{O}F(p) = \frac{1}{4} \int d\sigma(p') F(p') \frac{\mathcal{B}(p,p')}{\Omega(p) + \Omega(p')} \delta(p_1 + p_2 - p_1' - p_2').$$

P, H and L are self-adjoint operators and satisfy the commutation rules $[P, H] = 0$, $[P, L] = iH$ and $[H, L] = iP + O(\lambda^{2\nu})$ (see [6]). We thus have obtained a representation of the Poincaré group (on R^2 and at $O(\lambda^{2\nu})$) at zero-time with effective interaction (because of the existence of a bound state), which is deduced from the weakly-coupled $\mathcal{P}(\varphi)_2$ models.

References: [1] J. Glimm, A. Jaffe, *Quantum Physics*, Second edition, Springer Verlag (1987). [2] see the references in [3] and [5]. [3] E. Frochaux, *A variational proof of the existence of a bound state in Q.F.T.*, Helv. Phys. Acta, 61 (1988). [4] E. Frochaux, *The bound states in the weakly-coupled $\mathcal{P}(\varphi)_2$ models*, in preparation. [5] E. Frochaux, *Zero-time one-particle states in Q.F.T.*, to appear in Commun. Math. Phys. [6] E. Frochaux, A.-M. Moix, C. Raharinosy, *A quantum relativistic model for two interacting particles at zero-time*, in preparation.

The Nucleon – Nucleon Program at Saturne II

G. Gaillard[1], P. Bach[1], J. Ball[2], R. Binz[3], J. Bystricky[4], P. Demierre[1],
J.M. Fontaine[5], J.P. Goudour[6], R. Hess[1], A. Klett[3], R. Kunne[1],
C.D. Lac[2,4], F. Lehar[4], A. de Lesquen[4], D. Lopiano[7], M. de Mali[4],
F. Perrot[5], R. Peschina[3] , D. Rapin[1], E. Rössle[3], L. van Rossum[4],
H. Schmitt[3], P. Sormani[1] and H. Spinka[7].

[1] DPNC, University of Geneva, 1211 Geneva 4, Switzerland
[2] LNS, CEN-Saclay, 91191 Gif-sur-Yvette, France
[3] University of Freiburg, Freiburg im Brisgau, Germany
[4] DPhPE, CEN-Saclay, 91191 Gif-sur-Yvette, France
[5] DPhN/ME, CEN-Saclay, 91191 Gif-sur-Yvette, France
[6] University of Bordeaux, France
[7] ANL-HEP, Argonne, USA

The aim of the Nucleon–Nucleon program is to obtain the Nucleon–Nucleon amplitudes, either via Phase Shift Analyses or direct reconstruction. To this end, a large number of polarization observables, including spin transfer and 3-spin parameters, have been measured at Saturne II in neutron–proton elastic scattering, between 800 and 1100 MeV, using the free polarized neutron beam, obtained by breaking up of polarized deuterons. The analysis is still in a early stage, but, nevertheless, it has already been possible to reconstruct the neutron–proton amplitudes at 3 angles, at 840 and 880 MeV.

The Nucleon–Nucleon elastic scattering matrix is 4×4, but, if parity conservation, time reversal invariance and isospin invariance are assumed, the total number of independent complex amplitudes is reduced to 5 for each isospin state, I=0 or I=1. Since an overall phase is not experimentally reachable, one nead 9 real quantities (5 modules and 4 phases) for each isospin state to fully describe the scattering matrix which should be obtained by measuring 9 independent observables. In practice, to prevent ambiguities due to experimental uncertainties, more observables are required. One can get the isovector amplitudes from proton–proton elastic scattering measurements, since the proton–proton system is purely I=1 state. The neutron–proton elastic scattering amplitudes are a combination of isoscalar and isovector parts. Isoscalar NN amplitudes will then be obtained by substracting proton–proton amplitudes from neutron–proton's.

The first part of the Nucleon–Nucleon program was devoted to proton–proton elastic scattering from 800 to 2700 MeV and lead to a Phase Shift Analysis up to 1800 MeV[1] and to a direct amplitude reconstruction from 830 to 2700 MeV[2]. In the second part of the program, neutron–proton elastic scattering was studied at 5 energies between 800 and 1100 MeV. The polarized neutron beam was produced by breaking up of polarized deuterons delivered by the Saturne synchrotron on a 20 cm thick Be target. The neutron polarization was of 59 %. The polarized neutron were scattered on a frozen-spin polarized proton target. The typical proton polarization was 85%, with a relaxation time of 30 days in a 0.33 T field.

Spin dependent neutron–proton total cross sections $\Delta\sigma_L$ and $\Delta\sigma_T$ have been measured as well as 11 independent spin observables in the elastic scattering at each energy. Roughly one fourth of the data have been analysed and a direct reconstruction of the amplitudes have been performed at 3 angles at 840 and 880 MeV. Preliminary results of the reconstruction are shown below. The notations used are those from reference[3].

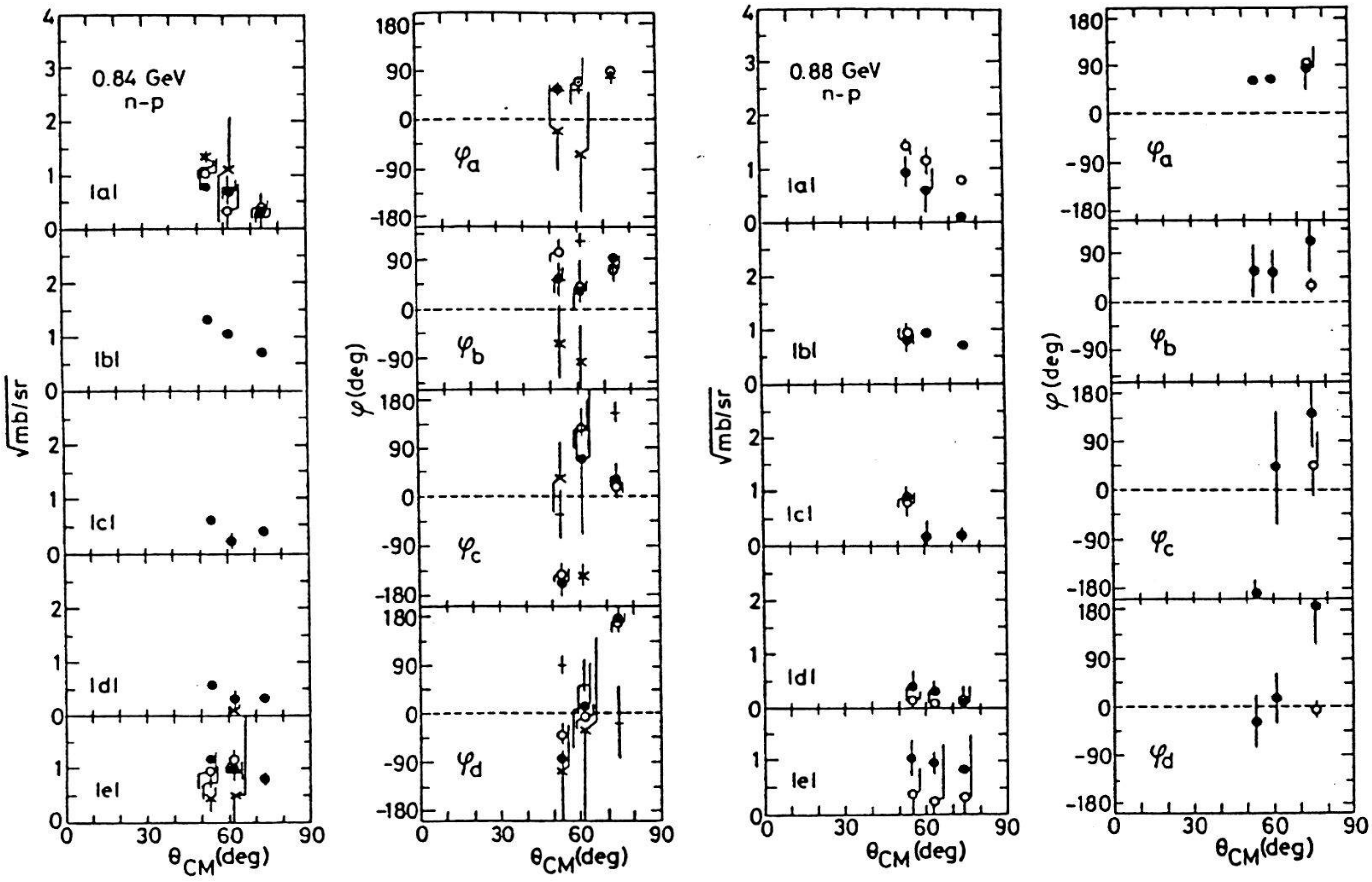

Four solutions were found at 840 MeV, one being less probable (×) than the others. At 880 MeV, two solutions were obtained. For one of them (o), the errors for the phases were larger than 180° at two angles, therefore, only the modules of the amplitudes are plotted.

References

[1] J. Bystricky, C. Lechanoine-Leluc, and F. Lehar. Phase shift analyses of pp elastic scattering at fixed energies between 0.83 and 1.8 GeV. to be published in *Journal de Physique* (Paris) Dec. 1990.

[2] C. D. Lac et al. Direct reconstruction of pp elastic scattering amplitudes from experimental data between 0.83 and 2.7 GeV. submitted to *Journal de Physique* (Paris).

[3] J. Bystricky, F. Lehar, and P. Winternitz. *Journal de Physique* (Paris), **39**(1978)1.

Comparison of Muon Transfer from Muonic Protium and Deuterium to Sulphur Dioxide

F. Mulhauser, R. Jacot-Guillarmod*, C. Piller, L.A. Schaller, L. Schellenberg and H. Schneuwly
Institut de Physique de l'Université, CH-1700 Fribourg, Switzerland

Abstract : Recent measurements of muon transfer from muonic hydrogen to sulphur and oxygen in a H_2+SO_2 gas mixture with natural hydrogen, showed unexpected and yet unexplained double-exponential time spectra of the muonic oxygen x-rays [1]. In order to test whether these surprising time spectra were related to the presence of deuterium, muon transfer in a D_2+SO_2 gas mixture was investigated. The unexpected phenomenon appears in the same manner in the deuterium mixture.

The muonic hydrogen atom is neutral and so small that it penetrates easily through the electron clouds of atoms, and can transfer its muon onto a muon-atomic orbit of other nuclei. The muon transfer rate can be measured by analyzing the time structure of the muonic x-rays following this transfer process [2].

In previous experiments [1,3,4], we measured the muon transfer from muonic hydrogen to sulphur and oxygen in H_2+SO_2 gas mixtures. These experiments were performed at different pressures and SO_2 concentrations. We observed that the time spectra of the sulphur x-rays had one decay constant, corresponding to the lifetime of the μp atom in the ground state. However, the time spectra of the oxygen x-rays had two time constants (Fig.1). The long time constant measured in the muonic oxygen x-rays transitions is the compatible with the one of the sulphur transitions.

In order to test whether these surprising time spectra were related to the presence of deuterium, muon transfer in a D_2+SO_2 gas mixture was investigated. One observed that the muonic sulphur x-ray time spectra of all the Lyman series transitions have only one time constant and that a double-exponential time distribution appears again in all muonic oxygen x-ray transitions (Fig. 2).

In the H_2+0.4%SO_2 gas mixture, the lifetime of the μp atom in the ground state, measured in the sulphur transitions, τ_S is equal to 107.0 (19) ns. This lifetime gives a reduced transfer rate from muonic hydrogen to sulphur dioxide of Λ_{pSO_2} = 2.51 (7) 10^{11} s^{-1} [4]. For the D_2+0.4%SO_2 measurement, performed in similar experimental conditions as the H_2+SO_2 experiment, we obtain for the lifetime of the μd atom in the ground state a value of 118 ns. This time constant is measured from the sulphur time spectra and appears also, as the long time constant on the oxygen time spectra. This lifetime gives a reduced transfer rate of Λ_{dSO_2} = 2.26 10^{11} s^{-1}. The short time constant, measured in all the oxygen x-rays time spectra of both experiments, is not the same for the two measurements. In the hydrogen gas mixture the time constant has a value of 40.9 (35) ns [4], and for the deuterium gas mixture, the value is of 26.2 ns. All these results are showed in the Table.

Table : Measured time constants and reduced transfer rates Λ_{SO_2}.

Mixture	Pressure [bar]	τ_1 [ns]	τ_2 [ns]	Λ_{pSO_2} $\cdot 10^{11}$ s^{-1}	Λ_{dSO_2} $\cdot 10^{11}$ s^{-1}
H_2+0.4%SO_2	14.9	107.0 19	40.9 35	2.51 7	
D_2+0.4%SO_2	15.0	118.1	26.2		2.26

The relative muonic x-ray intensities of the Lyman series, resulting from muons transferred from thermalized μp or μd atoms in the ground state to oxygen or to sulphur, can be predicted [5,6]. The intensity patterns of the delayed muonic oxygen x-rays, for the normal and the unexpected time component, agree with each other and with the prediction, for both hydrogen and deuterium gas mixtures. It is important to note that the muonic oxygen x-ray intensities, corresponding to the unexpected component have the same structure as if they would result from muon transfer from μp or μd atoms in the ground state.The ratio of the intensities of the unexpected component to the normal one is, for all four transitions, about 40%, for the H_2+0.4%SO_2 gas mixture. This ratio is smaller, about 30%, for D_2+0.4%SO_2.

The behaviour of the muon transfer from muonic hydrogen and from muonic deuterium seems to be the same. In each case, we observed an unexpected phenomenon, which remains unexplained, and the idea of "black" and "white" muonic atoms [7] has not yet been disproved.

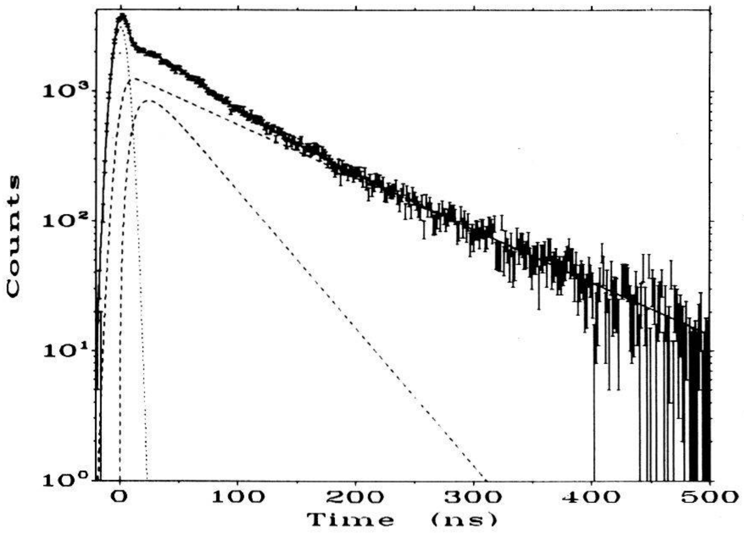

Figure 1 Measured and fitted time spectra of the muonic 2p-1s transition of oxygen in the H_2+0.4%SO_2 gas mixture.

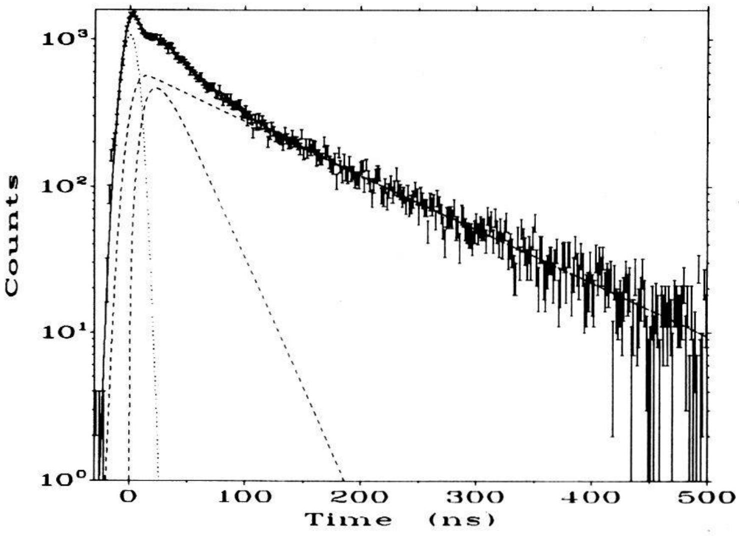

Figure 2 Measured and fitted time spectra of the muonic 2p-1s transition of oxygen in the D_2+0.4%SO_2 gas mixture.

* now at University of British Columbia, Vancouver, Canada.

References
[1] H. Schneuwly et al., Phys. Lett. A 132, 335 (1988)
[2] R. Jacot-Guillarmod et al., Phys. Rev. A 38, 6151 (1988).
[3] F. Mulhauser et al., Hel. Phys. Acta 63, 545 (1990)
[4] F. Mulhauser et al., Proceeding μCF 90' conference, Vienna
[5] S.S. Gershtein, Zh. Eksp. Teor. Fiz 43, 706 (1962) [Sov. Phys.-JETP 16, 501 (1963)]
[6] G. Holzwarth, H.J. Pfeiffer, Z. Phys. A 272, 311 (1975)
[7] H. Schneuwly, Muon Catalyzed Fusion 4, 87 (1989)

New measurements of Muon Transfer from Muonic Protium and Deuterium to Neon

R. Jacot-Guillarmod*, F. Mulhauser, C. Piller, L.A. Schaller, L. Schellenberg and H. Schneuwly
Institut de Physique de l'Université, CH-1700 Fribourg, Switzerland

Abstract : The new measurement of muon transfer from muonic protium to neon confirms the very low transfer rate observed in a preceding measurement. The new value for the transfer rate from muonic deuterium is only 2/3 of the older one, but remains one order of magnitude greater than the transfer rate from muonic protium.

Because of its small size and its electric neutrality a muonic hydrogen atom can easily cross electron clouds of atoms and approach the nuclei sufficiently to transfer its muon onto a muon-atomic orbit of nuclei with charge numbers $Z>3$. Corresponding muon transfer rates can, in principle, be easily measured by analyzing the time structure of the muonic x-rays following the transfer process [1,2].

In a recent measurement of muon transfer from muonic protium to neon [3], we observed a transfer rate which was about twenty times smaller than the one observed twenty years ago [1]. In addition, the time spectra of the muonic neon Lyman series x-rays in a H_2 + 0.7% Ne gas mixture, showed unexpected double-exponential structures similar but less pronounced to those observed in the muonic oxygen x-rays in H_2 + SO_2 gas mixtures [4].

The aims of the new measurements were to see whether the very low transfer rate from muonic protium to neon is confirmed and whether the transfer rate from muonic deuterium to neon is really one order of magnitude greater.

The comparison of the new measurements with the preceding ones is shown in the Table. The transfer rates are, as usual, normalized to the atomic density of liquid hydrogen. Only transfer rates measured in gaseous mixtures at room temperature are compared. The comparison shows that the very low transfer rate from muonic protium to neon is confirmed, although the new one is about 30 % higher.

The double-exponential structure of the time distributions of the muonic neon x-rays observed in the H_2 + 0.7% Ne gas mixture [3] is not reproduced in the H_2 + 1.4% Ne gas mixture of the present investigation. The new transfer rate from muonic deuterium to neon, which is only 2/3 of the older one, remains one order of magnitude greater than the transfer rate from muonic protium.

Table Comparison of normalized muon transfer rates from muonic protium, Λ_{pNe}, and muonic deuterium, Λ_{dNe}, to neon, measured in gaseous mixtures at room temperature.

Authors	Pressure [bar]	mixture	Λ_{pNe} [$\cdot 10^{11}$ s^{-1}]	Λ_{dNe} [$\cdot 10^{11}$ s^{-1}]
Alberigi Quaranta et al. [1]	26	H_2 + Ne + Xe	1.16 (28)	
Jacot-Guillarmod et al. [3]	15	H_2 + 0.7% Ne	1.15 (20)	
Jacot-Guillarmod et al. [3]	15	H_2 + 0.7% Ne	0.062 (4)	
Jacot-Guillarmod et al. [3]	15	H_2 + Ne +Ar	0.062 (5)	
This work	15	H_2 + 1.4% Ne	0.080 (4)	
Placci et al. [5]	6	D_2 + Ne		1.42 (20)
This work	15	D_2 + 0.45% Ne		0.97 (3)

The relative muonic x-ray intensities following muon transfer from the ground state of muonic hydrogen can be predicted and agree with the observation [2,3]. One expects that the main quantum number of the muon-atomic level in neon, to which the muon is transferred, is the same for both muonic protium and deuterium. In the measured intensity spectra of the muonic Lyman series in neon following muon transfer, one observes (cf. Figure) in D_2 + Ne the presence of a muonic Ne(7-1) transition which is absent in the H_2 + Ne mixtures. [3]. This difference is presently unexplained.

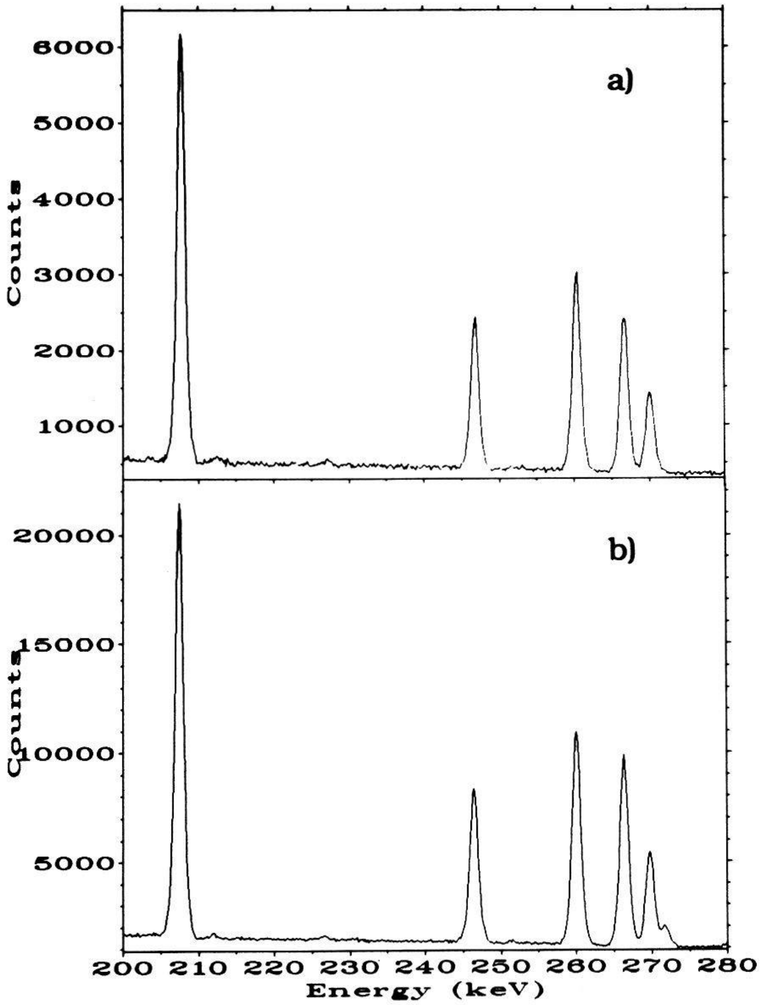

Figure Intensity spectra of the muonic Lyman series x-rays in neon following muon transfer from the ground state of muonic hydrogen measured at 15 bar in the mixtures : a) H_2 + 1.4% Ne, b) D_2 + 0.45% Ne.

* now at University of British Columbia, Vancouver, Canada.

References

[1] A. Alberigi Quaranta et al., Nuovo Cimento B 47, 92 (1967).
[2] R. Jacot-Guillarmod et al., Phys. Rev. A 38, 6151 (1988).
[3] R. Jacot-Guillarmod et al., Phys. Rev. Lett. 65, 709 (1990).
[4] H. Schneuwly et al., Phys. Lett. A 132, 335 (1988)
[5] A. Placci et al., Nuovo Cimento A52, 1247 (1967)

COMPLEXITY AND UNPREDICTABILITY OF NON-SELF-SIMILAR SCALING DYNAMICS

R. Badii and M. Finardi, Paul-Scherrer Institut, 5232 VILLIGEN
G. Broggi, Physik Institut der Universität, 8057 ZÜRICH-IRCHEL

Abstract: A system is regarded as complex if it reveals different features at each resolution level, in contrast to self-similar objects. We construct hierarchical models to extrapolate the asymptotic scaling properties exhibited by such systems under successive magnifications. Thermodynamic averages of the relevant observables are evaluated within a grand-canonical formalism and related to Feigenbaum's scaling functions. The convergence properties of the latter characterize the accuracy of the model and represent a measure of complexity.

1 Introduction

Spatio-temporal patterns exhibiting a high degree of organization are produced by a large number of physical systems, such as hydrodynamic flows, neural networks, living organisms, or by mathematical models like cellular automata, spin glasses and nonlinear dynamical systems. These structures are very often clearly distinct from both (quasi-) periodic and random-uncorrelated configurations. In particular, their macroscopic properties are not easily inferred from the observation of microscopic ones, or viceversa. The task of building a model for the underlying dynamics, able to yield patterns "statistically" equivalent to the original one, is then rather "complex" since it may require an infinity of different coarse-graining steps. We construct hierarchical models (trees) which describe the relationships among observable values measured at different resolution scales and use them to predict the asymptotic scaling of the system from the available non-asymptotic data. This global, hierarchical, approach should not be confused with that involving predictions of local behaviour, such as the conformation of a neighbourhood (either in time or space) of the currently scanned region in the pattern [1].

2 Thermodynamic Averages and Scaling Functions

Continuous configurations can be discretized by suitably partitioning the state-space. The analysis is then performed on the (one-dimensional) symbolic signal $\mathcal{S} = s_1 s_2 \ldots$ thus obtained. Hence, spin systems (including cellular automata) and generic dynamical systems can be treated within the same formalism. After splitting the signal $\mathcal{S}$ into "primitive" words w which satisfy suitable recurrence conditions [1], the underlying dynamics is described by a tree on which all allowed transitions among substrings $S = w_i w_j \ldots$ of $\mathcal{S}$ are recorded. The tree is dressed by associating to each sequence S the value $Q(S)$ of a physical observable (e.g., its probability $P(S)$ or its length $|S|$). The asymptotic properties of the system are then studied through the behaviour of "thermodynamic sums"[2,3] like, e.g., $\Omega_l(z;\beta) = \sum_{\text{level } l} z^{|S|} P^{\beta}(S)$, evaluated at each level l of the tree, for $l \to \infty$. This corresponds to a grand-canonical representation since, in general, strings with different lengths $|S|$ are considered. The extrapolation for $l \to \infty$ is made by estimating the leading eigenvalue of the transfer matrix

$$\mathbf{T}(z): \quad T_{w_0 w_1' \ldots w_l'; w_1 \ldots w_{l+1}} \equiv \sigma_{l+1}^{\beta}(w_0 w_1 \ldots w_{l+1}) z^{|w_{l+1}|} \delta_{w_1' w_1} \cdot \ldots \cdot \delta_{w_l' w_l} \,, \tag{1}$$

where $\sigma_{l+1}(w_0 w_1 \ldots w_{l+1}) \equiv P(w_0 w_1 \ldots w_{l+1}) / P(w_0 w_1 \ldots w_l)$ is a term of a generalized level-$(l{+}1)$ probability scaling function[3]. The matrix $\mathbf{T}(z)$ describes the conditional probability of the transition between the strings $w_0 w_1' \ldots w_l'$ and $w_1 w_2 \ldots w_{l+1}$, upon shifting by one primitive. The accuracy of the model and the speed of convergence of the thermodynamic sums are measured by the complexity $C_1 = \lim_{l \to \infty} \langle \ln(\sigma_{l+1}/\sigma_l) \rangle$: they depend on the range of the correlations in $\mathcal{S}$ and on the topology of the tree. It is then natural to associate the concept of "complexity" to systems whose coarse-grain (large $|S|$) properties cannot be accurately predicted from those measured at finer scales (or viceversa, in phase-space X). The primitives $w_1, w_2, \ldots$ can be recoded into symbols from a new alphabet $A' = \{0, 1, \ldots\}$ and the whole analysis can be repeated on the transformed string $\mathcal{S}'$ thus obtained. Upon iteration, one obtains a progressive coarse-graining of the symbolic signal (increased resolution in phase-space) and more accurate estimates. This approach has been applied to several dynamical systems and will be extended to the analysis of experimental time series[1]. The knowledge of the allowed transitions on the tree can be exploited to construct local models to predict the usual time-dynamics as well.

3 References

[1] R. Badii in *"Measures of Complexity and Chaos"*, N.B. Abraham et al. Eds., Plenum, New York (1990); R. Badii, M. Finardi and G. Broggi, in *"Information Dynamics"*, H. Atmanspacher, H. Scheingraber and R. Treumann Eds., Plenum, New York (1991); R. Badii, M. Finardi and G. Broggi, in *"Chaos, Order and Patterns"*, A. Artuso et al. Eds., Plenum, New York (1991); R. Badii, M. Finardi, G. Broggi and M.A. Sepúlveda, to be published.

[2] D. Ruelle, *"Thermodynamic Formalism"*, Encyclopedia of Mathematics and its Applications, Addison-Wesley, Reading (1978).

[3] M.J. Feigenbaum, J. Stat. Phys. **52**, 527 (1988).

GLOBAL MODEL CONSTRUCTION FROM EXPERIMENTAL DATA

R. Badii and M. Finardi, Paul-Scherrer Institut (LUS), 5232 VILLIGEN

Abstract: We present a program for the analysis of experimental aperiodic time-series. By localizing all unstable periodic orbits (up to a given order), a Poincaré section and an approximate generating partition are determined in the embedding space. The resulting symbolic dynamics is condensed into a hierarchical model which is able to produce signals statistically equivalent to the actual one. Local maps can be constructed to approximate the full continuous-time evolution in the embedding space between consecutive returns on the Poincaré section.

1 Introduction

The hierarchical modelling procedure for nonlinear flows, presented in Refs.([1,2]), is extended to the analysis of experimental aperiodic time-series. The aim is to derive a global model which can generate signals with the same statistical properties (expectation values, correlation functions) as the original one. In addition to this, it is also possible to construct local maps to be used as predictors for the short-time future evolution of the system. Once a phase-space representation is obtained by embedding the data in an E-dimensional space, the topological invariants (unstable periodic orbits) are localized in the neighbourhood of trajectories which close onto themselves to within a given accuracy ε. The latter depends on the number N of available data points, on the local attractor's dimension α, on the velocity in the embedding space along the current orbit and on the embedding dimension E. A (possibly disconnected) surface of section Σ is then chosen in such a way that it intersects all detected periodic orbits. In this way, time is discretized and all "period-n" orbits are assigned the same topological return time (n intersections). A partition of Σ is then obtained by choosing domains Δ_i around the shortest periodic orbits and by labelling them with integers $i = 0, 1, \ldots$. Longer orbits are classified according to the indices of the domains Δ intersected by them on Σ. The partition is subsequently modified until a different encoding is achieved for each periodic point lying on Σ. Hence, the original continuous dynamics is mapped onto a subshift on a symbolic sequence $S = s_1 s_2 \ldots$ and is modelled by means of a logic tree which records all admissible orbit-to-orbit transitions, as described in[2].

2 Applications

We have first studied scalar time-series obtained by integrating the Lorenz and Duffing differential flows, both in the presence of intrinsic and "instrumental" noise, sampled with a 12-bit resolution. The data were embedded in 3- to 15-dimensional spaces. A number $N = 5 \cdot 10^5$ of points has been generated, separated by a sampling time τ of the order of $1/25$ of the shortest periodic orbit in the system. All orbits up to order $n = 7$ have been extracted and compared with those determined by a direct study of the differential equations, for various parameter values. After a Poincaré section has been chosen, the attractor on it has been compared with that of the differential flow, to test the reliability of the method. For non-autonomous systems, like Duffing's equation, a Poincaré section can be found exactly also in the embedding space, by taking points separated by one period T of the forcing term, thus allowing for an additional test. The same procedure has then been applied to chaotic signals produced by a periodically driven NMR-laser[3]. The resulting logic-tree description[2] has been turned into a sequence of Markov models which have been used to explain the structure of the power spectra and to evaluate the asymptotic behaviour of the "thermodynamic sums"[4] yielding generalized dimensions, entropies and Lyapunov exponents with a much superior accuracy than that achievable by methods based on usual time-averages.

Finally, linear maps are constructed for each symbolic sequence (domain Δ) allocated on the tree and used to predict the local time evolution of the system for one return time on the Poincaré section. The method will be generalized to include fully nonlinear transformations, in order to reproduce possible singularties in the invariant measure. Procedures to smoothen data corrupted by noise are under development.

3 References

[1] G. Broggi, R. Badii and M. Finardi, Helv.Phys. Acta **63**, 815 and 817 (1990).

[2] R. Badii, M. Finardi and G. Broggi, *"Complexity and Unpredictability of Non-self-similar Scaling Dynamics"*, this issue.

[3] E. Brun, B. Derighetti, D. Meier, R. Holzner and M. Ravani, J.Opt.Soc.Am. **B2**, 156 (1985).

[4] D. Katzen and I. Procaccia, Phys.Rev.Lett. **58**, 1169 (1987);
P. Grassberger, R. Badii and A. Politi, J.Stat.Phys. **51**, 135 (1988);
R. Badii, Riv. Nuovo Cim. **12**, N° 3, 1 (1989);
R. Artuso, E. Aurell and P. Cvitanović, Niels Bohr Institute preprints NBI-89-41 and NBI-89-42.

Helvetica Physica Acta
Vol. 64 (1991)

0018-0238/91/020211-01$1.50+0.20/0

Editors' note

on the paper

"A non-relativistic supersymmetric two-body equation
for scalar and spinor particles"

by Fu-bin Li, published in Helv. Phys. Acta 63, 922 (1990)

Profs. Z. Aydin and U. Yilmazer have informed us that the above-mentioned article is identical practically word by word with their own paper "Euclidean supersymmetry and relativistic two-body systems" which appeared almost three years ago in Nuovo Cimento 99 A, 85 (1988).

This fact escaped both the referee and the editor. We regret this unfortunate circumstance, and we cannot but condemn the inadmissible practice of claiming authorship of duplicated material.